Observations of the vertical distributions of summertime atmospheric pollutants in Nam Co: OH production and source analysis

Chengzhi Xing[1], Cheng Liu[1,2,3,4,*], Chunxiang Ye[5,*], Jingkai Xue[6], Hongyu Wu[6], Xiangguang Ji[7], Jinping Ou[8], and Qihou Hu[1]

[1] Key Lab of Environmental Optics & Technology, Anhui Institute of Optics and Fine Mechanics, Hefei Institutes of Physical Science, Chinese Academy of Sciences, Hefei, 230031, China

[2] Department of Precision Machinery and Precision Instrumentation, University of Science and Technology of China, Hefei, 230026, China

[3] Center for Excellence in Regional Atmospheric Environment, Institute of Urban Environment, Chinese Academy of Sciences, Xiamen, 361021, China

[4] Key Laboratory of Precision Scientific Instrumentation of Anhui Higher Education Institutes, University of Science and Technology of China, Hefei, 230026, China

[5] College of Environmental Sciences and Engineering, Peking University, 100871 Beijing

[6] School of Environmental Science and Optoelectronic Technology, University of Science and Technology of China, Hefei, 230026, China

[7] Institute of Physical Science and Information Technology, Anhui University, Hefei, 230601, China

[8] The Department of Health Promotion and Behavioral Sciences, School of Public Health, Anhui Medical University, Hefei, 230032, China

*Corresponding author. E-mail: chliu81@ustc.edu.cn; c.ye@pku.edu.cn

1 **Abstract**

2 The Tibetan Plateau (TP) plays a key role in regional environment and global climate change, however,
3 the lack of vertical observation of atmospheric species, such as HONO and O_3, hinders a deeper
4 understanding of the atmospheric chemistry and atmospheric oxidation capacity (AOC) on the TP. In
5 this study, we conducted multi-axis differential optical absorption spectroscopy (MAX-DOAS)
6 measurements at Nam Co, the central TP, to observe the vertical profiles of aerosol, water vapor (H_2O),
7 NO_2, HONO and O_3 from May to July 2019. In addition to NO_2 mainly exhibiting a Gaussian shape
8 with the maximum value appearing at 300-400 m, other four species all showed an exponential shape
9 and decreased with the increase of height. The maximum values of monthly averaged aerosol (0.17
10 km^{-1}) and O_3 (66.71 ppb) occurred on May, H_2O (3.68×10^{17} molec cm^{-3}) and HONO (0.13 ppb)
11 appeared on July, while NO_2 (0.39 ppb) occurred on June at 200-400 m layer. H_2O, HONO and O_3 all
12 exhibited a multi-peak pattern, and aerosol appeared a bi-peak pattern for their averaged diurnal
13 variations. The averaged vertical profiles of OH production rates from O_3 and HONO all exhibited an
14 exponential shape decreasing with the increase of height with maximum values of 2.61 ppb/h and 0.49
15 ppb/h at the bottom layer, respectively. The total OH production rate contributed by HONO and O_3 on
16 the TP was obviously larger than that in low-altitude areas. In addition, source analysis for HONO and
17 O_3 at different height layers were conducted. The heterogeneous reaction of NO_2 on wet surfaces was a
18 significant source of HONO. The maximum values of HONO/NO_2 appeared around H_2O being $1.0 \times$
19 10^{17} molec cm^{-3} and aerosol being lager 0.15 km^{-1} under 1.0 km, and the maximum values usually
20 accompanied with H_2O being 1.0-2.0×10^{17} molec cm^{-3} and aerosol being lager 0.02 km^{-1} at 1.0-2.0 km.
21 O_3 was potentially sourced from south Asian subcontinent and Himalayas through long-range transport.
22 Our results enrich the new understanding of vertical distribution of atmospheric components and
23 explained the strong AOC on the TP.

24

25 **1 Introduction**

26 The TP spans 2.5 million square kilometers with an average altitude of over 4000 m. Therefore, the TP
27 is called the "Third Pole" of the earth (Ma et al., 2020; Kang et al., 2022). It is the home to tens of
28 thousands of glaciers and nourishes more than 10 of Asia's rivers, thus it also acts the role of "Water
29 Tower of Asia" (Qu et al., 2019; Ma et al., 2022). Due to its special topography, the TP is the heat
30 source of atmosphere due the strong solar radiation, which as the driven force to profoundly affect the
31 regional atmospheric circulation, global weather conditions and climate change (Yanai et al., 1992;
32 Boos et al., 2010; Chen et al., 2015; Liu et al., 2022; Zhou et al., 2022). Monsoon rainfall in Asia, flood
33 over the Yangtze River valley, and El Niño in the Pacific Ocean are strongly associated with the TP
34 (Hsu et al., 2003; Li et al., 2016; Lei et al., 2019). In addition, the cyclone circulations caused by the
35 TP heat source also can inhibit the diffusion of atmospheric pollutants in the areas around the TP, such
36 as the Sichuan Basin, causing regional pollution (Zhang et al., 2019). Therefore, observations of the
37 atmospheric species on the TP are essential to enhance the in-depth understanding of its atmospheric
38 physicochemical processes.

39 However, deciphering the atmospheric environment of the TP is highly challenging and dangerous, due
40 to its complex topography and harsh environment (Barnett et al., 2005; Bolch et al., 2012; Cong et al.,
41 2015; Kang et al., 2016). In order to unveil the feature of atmospheric composition over the TP and
42 their corresponding climate feedback, a large number of field observation stations have been
43 established, and a series of field campaigns have continued to be carried out recently, especially after
44 the performance of "the Second Tibetan Plateau Scientific Expedition and Research Program" (Che and
45 Zhao 2021; Wang et al., 2021; Ran et al., 2022). The China National Environmental Monitoring Center
46 (CNEMC) has established an in-situ monitoring network with more than 12 stations over the TP, such
47 as Lhasa, Shigatse, Shannan, Nyingchi, Nagqu, Ngari, Qamdo, Diqing, Aba, Guoluo, Xining, and
48 Haixi, to continuously monitor the surface concentrations of six atmospheric components (i.e. PM_{10},
49 $PM_{2.5}$, NO_2, SO_2, O_3 and CO) since 2013 (Gao et al., 2020; Li et al., 2020; Sun et al., 2021). The
50 Institute of Tibetan Plateau Research, Chinese Academy of Sciences, has also established six long-term
51 field observation stations to measure meteorological parameters and small amounts of atmospheric
52 composition (i.e. black carbon, aerosol optical density (AOD)) (Ma et al., 2020). In addition, scientists
53 are relying on advancements in satellite remote sensing technology, such as the tropospheric
54 monitoring instrument (TROPOMI), the ozone monitoring instrument (OMI), the moderate-resolution
55 imaging spectroradiometer (MODIS) and the cloud-aerosol lidar and infrared pathfinder satellite
56 observation (CALIPSO), to monitor the spatial and temporal evolutions of atmospheric composition on
57 the TP (Zhu et al., 2019; Li et al., 2020; Rawat and Naja 2022). Their advantage is to obtain the column
58 densities of pollutants in a large-scale space of the TP. Although CALIPSO could detect aerosol
59 vertical profiles, the spatiotemporal resolution (i.e. ~5.0 km horizontal resolution, 0.06 km vertical
60 resolution and ~16 d temporal resolution) is limited and the data uncertainty in the planetary boundary
61 layer (PBL) is large due to the low signal-to-noise ratio (Huang et al., 2007). However, several studies
62 also revealed that the formation, aging and transport processes of atmospheric composition on the TP
63 occurs not only near the ground surface but also at high altitudes (Xu et al., 2020; Xu et al., 2022). The
64 high PBL on the TP caused by its strong solar radiation and undulating terrain promotes the
65 atmospheric exchange between the bottom troposphere and stratosphere (Yang et al., 2003; Seidel et al.,
66 2010). Therefore, the lack of vertical profiles of hinders the understanding of the evolution of trace
67 gases and their environmental and climate effects over the TP. In recent years, balloon and lidar
68 vertical measurements on the TP are occasionally carried out (Fang et al., 2019; Zhang et al., 2020;
69 Dong et al., 2022), but their limited detection species (i.e. aerosol and O_3) and high cost are obstacles
70 that limit long-term continuous observation and the conduction of more in-depth scientific research.
71 MAX-DOAS has the technical advantage of low-cost continuous observation of multiple atmospheric
72 components (i.e. aerosol, O_3 and their precursors) (Wang et al., 2018; Ma et al., 2020; Cheng et al.,
73 2021; Xing et al., 2021; Li et al., 2022; Cheng et al., 2023a, 2023b). Combining these data with better
74 scientific models can reduce the modeling bias and promote to better understand the physical, chemical
75 and dynamical processes.

76 The strong convergent airflow formed under the combined action of monsoon, subtropical anticyclone
77 and the airflow of subtropical westerlies could promote the accumulation of O_3 on the TP in summer

78 (Ye and Gao 1997). Therefore, several studies have revealed the high O_3 concentration on the TP (Li et
79 al., 2022; Yang et al., 2022; Yu et al., 2022). The strong solar radiation, high O_3 concentration and
80 relatively high humidity on the TP provide great potential for high OH production. Lin et al. (2008) and
81 Ye (2019) also confirmed that the high OH over the TP is mainly related to the reaction between $O(^1D)$
82 and H_2O. The $O(^1D)$ is produced from the photolysis of O_3 by UV radiation. Therefore, a hypothesis of
83 "strong AOC over the TP" was put forward. Previous studies pointed out that HONO also play an
84 important role in AOC at low-altitude areas, and its contribution to OH can reach 40-60%, and even
85 more than 80% in the early morning (Michoud et al., 2012; Ryan et al., 2018; Xue et al., 2020).
86 However, few HONO studies on the TP have been reported. Our previous study operated at the
87 Qomolangma Atmospheric and Environmental Observation and Research Station, Chinese Academy of
88 Sciences (QOMS-CAS) revealed that the HONO mainly distributed in the lower PBL and peaked in
89 summer with 1.11 ppb, which is comparable to the average level of HONO in other low-altitude areas
90 (Luo et al., 2010; Xing et al., 2021a, 2021b; Yang et al., 2021). It indicates that it is also necessary to
91 study the contribution of HONO to AOC on the TP. Furthermore, understanding the vertical
92 distribution of OH is of great significance for learning about the atmospheric chemical processes and
93 the evolution of atmospheric components on the TP (Zhou et al., 2015). Identifying the sources of O_3
94 and HONO is the basis for studying the AOC on the TP. The limited researches concluded that the
95 atmospheric HONO on the TP is mainly sourced from the emissions of vehicles, biomass burning and
96 soil, except for the NO_2 heterogeneous reaction on aerosol surfaces (Xing et al., 2021). The lower
97 tropospheric O_3 on the TP is mainly dominated by local photochemical reactions, regional horizontal
98 transport, vertical mixing and the intrusion from stratosphere (Yin et al., 2017; Xu et al. 2018).

99 In this study, we firstly analyzed the temporal and vertical characteristics of several atmospheric
100 components (i.e. aerosol, H_2O, NO_2, HONO and O_3) based on MAX-DOAS observations in Nam Co.
101 Afterwards, the contributions of O_3 and HONO to OH in the vertical space were discussed through the
102 tropospheric ultraviolet and visible (TUV) radiative transfer model and MAX-DOAS measurements.
103 Finally, the potential sources of O_3 and HONO at different altitudes were analyzed based on the
104 MAX-DOAS retrievals.

105 2 Method and methodology

106 2.1 Site

107 The Nam Co Monitoring and Research Station for Multisphere Interactions, CAS (NAMORS)
108 (30.774ºN, 90.988ºE; 4730 m a.s.l.) is located at the southeast banks of Nam Co lake and the foothills
109 of the northern Mt. Nyainqêntanglha (Fig. 1). The station land is covered by alpine meadows with soil
110 type of sandy silt loam. The southwest monsoon can carry abundant moisture from Indian Ocean to this
111 station in summer to increase humidity and precipitation there. Moreover, due to the summertime huge
112 evaporation from Nam Co lake, the atmospheric H_2O around CAS (NAMORS) is more abundant than
113 in other areas of the TP, resulting in lush grass vegetation and making the area around this station an
114 important summertime pasture. In addition, there are not large industries and cities within 100 km of
115 the CAS (NAMORS). The closest town to CAS (NAMORS) is Dangxiong county which is about 60
116 km away from this station and lower about 500 m than this station. Only a small number of vehicles
117 pass through this area during summer tourism season. Therefore, no obvious anthropogenic sources of
118 air pollutants exist near this station. Averaged spatial distributions of AOD, O_3, NO_2 and HCHO
119 monitored by satellite from May to July 2019 are shown in Figure S1. Elevated AOD, NO_2, and O_3 are
120 mainly distributed in South Asian subcontinent (e.g. India and Nepal), the southern foothills of the
121 Himalayas, which is located in the upwind direction of the southwest monsoon potentially affecting the
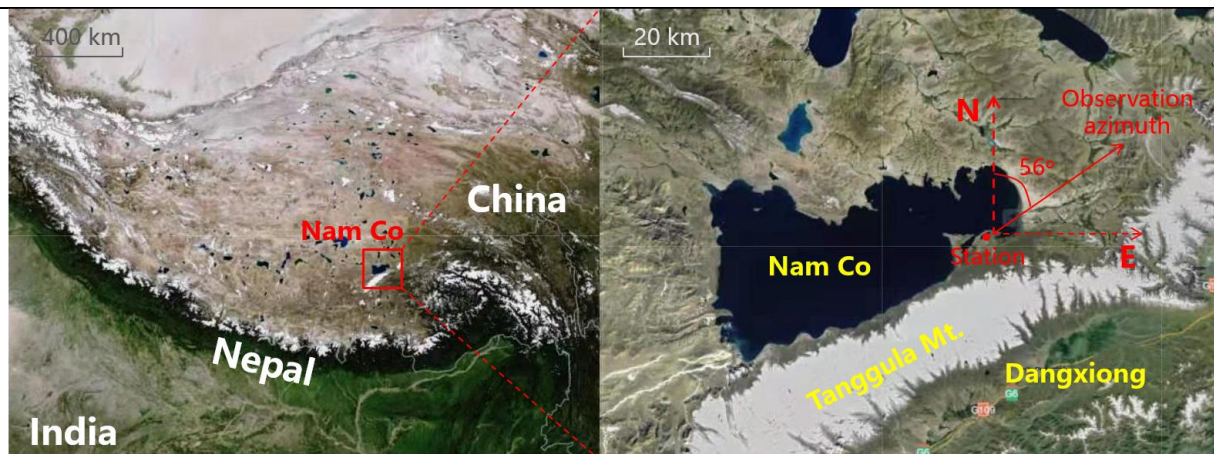122 atmospheric composition over CAS (NAMORS).

123

124   Figure 1. Geographical location of CAS (NAMORS) on the Tibet plateau.

125 **2.2 Measurements**

126 2.2.1 Instrument setup and spectral analysis

127 The MAX-DOAS instrument installed at CAS (NAMORS) was operated from 01 May to 09 July 2019.
128 It consists of three major parts: telescope unit, spectrometer unit and control unit. The detailed
129 description of this instrument can be found in Xing et al. (2021). In this study, the elevation angle
130 sequence was set to 1, 2, 3, 4, 5, 6, 8, 10,15, 30, and 90° with an exposure time of 60 s to each
131 individual spectrum. The azimuth angle was set to 56° pointing to Nagqu direction. Moreover, only
132 spectra collected under solar zenith angle (SZA) less than 75° was used for spectral analysis to avoid
133 the strong stratospheric absorption.

134 The differential slant column densities (DSCDs) of O_4, H_2O, NO_2, HONO and O_3 were retrieved using
135 QDOAS software (http://uvvis.aeronomie.be/software/QDOAS/) developed by Royal Belgian Institute
136 for Space Aeronomy (BIRA-IASB). The zenith spectrum measured at every sequence were selected as
137 scan Frauenhofer reference spectrum. The retrieval configurations of O_4, H_2O, NO_2, HONO and O_3
138 followed Xing et al. (2017), Lin et al. (2020), Xing et al. (2021), Wang et al. (2020) and Wang et al.
139 (2018), respectively. The detailed DOAS fit settings of above five species were listed in Table 1.
140 Corrected I_0 (Aliwell et al., 2002) was used in this study. Fig. 2 shows a typical DOAS retrieval
141 example for above five species. DOAS fit results with root mean square (RMS) values larger than $5\times$
142 10^{-4}, 5×10^{-4}, 5×10^{-4}, 1×10^{-3}, and 6×10^{-4} for O_4, H_2O, NO_2, HONO, and O_3, respectively, were
143 filtered out. In addition, we calculated color index (CI) to remove cloud effect (Wagner et al., 2016).
144 The data filter criteria according to CI followed by Ryan et al. (2018) and Xing et al. (2020).
145 Afterwards, the quantified DSCDs of O_4, H_2O, NO_2, HONO, and O_3 remained 91.33%, 91.97%,
146 92.16%, 86.42% and 81.09%, respectively.

147 2.2.2 Vertical profile retrieval

148 The vertical profiles of aerosol and trace gases (i.e. H_2O, NO_2, HONO and O_3) were retrieved using
149 algorithm based on optimal estimation method (OEM). A linearized pseudo-spherical vector discrete
150 ordinate radiative transfer model VLIDORT was used as forward model and a Gauss-Newton (GN)
151 scheme was used as the inversion strategy (Wedderburn et al., 1974). The detailed description of this
152 algorithm can be found in Liu et al. (2021), Xing et al. (2021) and Wang et al. (2018). The detailed
153 retrieval processes were depicted in Sect. S1 of the supplement. In this study, the initial a priori profile
154 shape of above five species was set to exponential decreasing shape, and the AOD and vertical column
155 densities (VCDs) simulated by weather research and forecasting model coupled chemistry (WRF-Chem)
156 were also used as initial input a priori information to constrain the retrieval process. For the O_3 profile
157 retrieval, the stratospheric O_3 profile was deducted using TROPOMI O_3 profile (Zhao et al., 2021). We
158 set 20 vertical layers from 0.0 to 4.0 km with a vertical resolution of 0.2 km. The correlation height was
159 set to 1.0 km. Moreover, the surface albedo, single scattering albedo and asymmetry parameter were set
160 to fixed constant of 0.08, 0.85 and 0.65, respectively (Irie et al., 2008). The retrieved vertical profiles

4

were removed under the condition of degree of freedom (DOF) and relative error less than 1.0 and
100%, respectively.

Table 1. Detailed DOAS retrieval settings for O_4, H_2O, NO_2, HONO and O_3.

Parameter	Data source	Fitting intervals (nm)				
		O_4	H_2O	NO_2	HONO	O_3
Wavelength range		338-370	433-455	338-370	340-373	320-340
NO_2	298K, I_0-corrected, Vandaele et al. (1998)	√	√	√	√	√
NO_2	220K, I_0-corrected, Vandaele et al. (1998)	√	√	√	√	×
O_3	223K, I_0-corrected, Serdyuchenko et al. (2014)	√	√	√	√	√
O_3	243K, I_0-corrected, Serdyuchenko et al. (2014)	√	×	√	√	×
O_3	293K, I_0-corrected, Serdyuchenko et al. (2014)	×	×	×	×	√
O_4	293K, Thalman and Volkamer (2013)	√	√	√	√	√
HCHO	298K, Meller and Moortgat (2000)	√	×	√	√	√
Glyoxal	298K, Volkamer (2005)	×	√	×	×	×
H_2O	HITEMP (Rothman et al. 2010)	√	√	√	√	×
BrO	223K, Fleischmann et al. (2004)	√	×	√	√	×
HONO	296K, Stutz et al. (2000)	×	×	×	√	×
Ring	Calculated with QDOAS	√	√	√	√	√
Polynomial degree		Order 3	Order 3	Order 3	Order 5	Order 3
Intensity offset		Constant	Constant	Constant	Constant	No

164
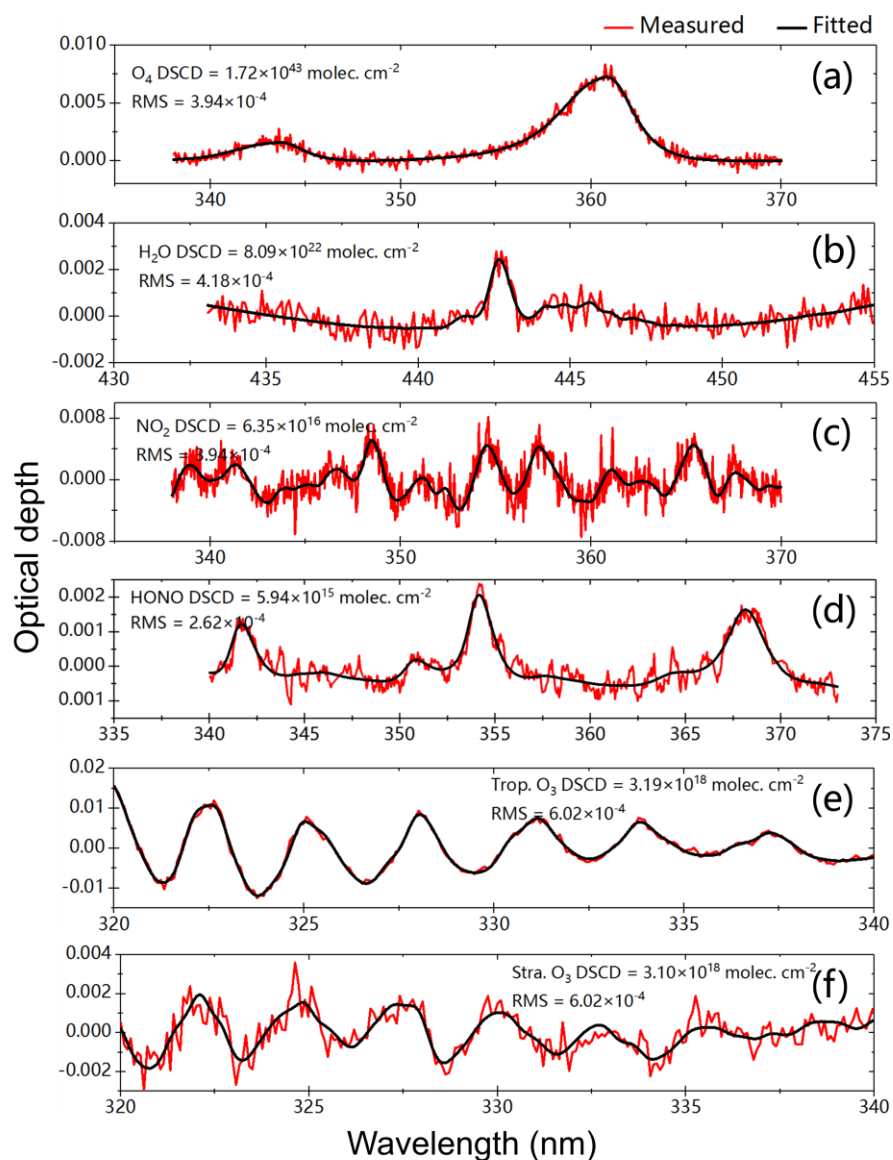
Figure 2. DOAS fit examples of O_4, H_2O, NO_2, HCHO, tropospheric O_3 and stratospheric O_3. The red line and black line represent the measured and fitted results, respectively.

2.2.3 Error analysis

The error sources can be divided into four different types: smoothing error, noise error, forward model error, and model parameter error (Rodgers, 2004). However, in terms of this classification, some errors are difficult to be calculated or estimated. For example, the forward model error, which is caused by an imperfect representation of the physics of the system, is hard to be quantified due to the difficulty of acquiring an improved forward model. Given calculation convenience and contributing ratios of different errors in total error budget, we mainly took into account following error sources, which were smoothing and noise errors, algorithm error, cross section error, and uncertainty related to the aerosol retrieval (only for trace gas). In this study, we estimated the contribution of different error sources to the AOD and VCDs of trace gases, and near-surface (0–200 m) trace gases' concentrations and aerosol extinction coefficients (AECs), respectively. The detailed demonstrations and estimation methods are displayed below.

a. Smoothing errors arise from the limited vertical resolution of profile retrieval. Noise errors denote the noise in the spectra (i.e., the error of DOAS fits). Considering the error of the retrieved state vector equaling the sum of these two independent errors, we calculated the sum of smoothing and noise errors on near-surface concentrations and column densities, which were 13 and 5 % for aerosols, 13 and 36 % for H_2O, 12 and 14 % for NO_2, 18 and 21 % for HONO, and 12 and 32 % for O_3, respectively.

b. Algorithm error is denoted by the differences between the measured and simulated DSCDs. This error contains forward model error from an imperfect approximation of forward function, parameter error of forward model, and other errors, such as detector noise (Rodgers, 2004). Algorithm error is a function of the viewing angle, and it is difficult to assign this error to each altitude. Thus, this error on the near-surface values and column densities is estimated through calculating the average relative differences between the measured and simulated DSCDs at the minimum and maximum elevation angle (except 90°), respectively (Wagner et al., 2004). In this study, we estimated these errors on the near-surface values and the column densities at 4 and 8 % for aerosols, 3 and 11 % for NO_2, and 20 and 20 % for HONO referring to Wang et al. (2017, 2020), 1 and 8 % for H_2O referring to Lin et al. (2020), and 6 and 10 % for O_3 referring to Ji et al. (2023), respectively.

c. Cross section error arises from the uncertainty in the cross section. According to Thalman and Volkamer, (2013), Lin et al. (2020), Vandaele et al. (1998), Stutz et al. (2000), and Serdyuchenko et al. (2014), we adopted 4, 3, 3, 5, and 2 % for O_4 (aerosols), H_2O, NO_2, HONO and O_3, respectively.

d. The profile retrieval error for trace gases is sourced from the uncertainty of aerosol extinction profile retrieval and propagated to trace gas profile. This error could be roughly estimated based on a linear propagation of the total error budgets of the aerosol retrievals. The errors of the learned four trace gases were roughly estimated at 14 % for VCDs and 10 % for near-surface concentrations, respectively.

The total uncertainty was the sum of all above errors in the Gaussian error propagation, and the error results were listed in Table 2. We found that the smoothing and noise errors played a dominant role in the total uncertainties of aerosol and trace gases. Moreover, improving the accuracy and temperature gradient of the absorption cross section is another important means to reduce the uncertainty of the vertical profiles in the future, especially for O_3.

Table 2. Error budget estimation (in %) of the retrieved near-surface (0–200 m) concentrations of trace gases and AECs, and AOD and VCDs.

		Error sources				Total
		Smoothing and noise errors	Algorithm error	Cross section error	Related to the aerosol retrieval	
Near-surface	aerosol	13	4	4	/	14
	H_2O	13	1	3	14	19
	NO_2	12	3	3	14	18
	HONO	18	20	5	14	29

6

	O_3	12	6	2	14	19
VCD or AOD	AOD	5	8	4	/	10
	H_2O	36	8	3	10	38
	NO_2	14	11	3	10	20
	HONO	21	20	5	10	31
	O_3	32	10	2	10	35

211

2.3 TUV model

213 The calculation of photolysis rates of HONO and O_3 used TUV radiation model
214 (https://www2.acom.ucar.edu/modeling/tropospheric-ultraviolet-and-visible-tuv-radiation-model)
215 based on a full FORTRAN code. In order to ensure the accuracy of model running, we only selected
216 data in sunny and cloudless days. Moreover, we developed a cloud classification method based on the
217 diurnal variations of Color Index (CI=I_{330}/I_{360}) in Figure S2. The initial input parameters were as
218 follows: the AOD at 361 nm was derived from aerosol extinction profiles measured by MAX-DOAS;
219 the daily total ozone column density was measured by TROPOMI with a value range of 260-280 DU;
220 the single scattering albedo (SSA) was calculated based on the regression analysis of multi-wavelength
221 (361 and 477 nm) O_4 absorptions measured by MAX-DOAS (Xing et al., 2019); fixed Ångström
222 exponents of 0.508, 0.581 and 0.713 were used in May, June and July, respectively, referring to Xia et
223 al. (2011).

2.4 Backward trajectory, PSCF and CWT analysis

225 The 48-h backward trajectories at five heights of 200, 600, 1000, 1400 and 1800 m were calculated
226 using the Hybrid Single-particle Lagrangian Integrated Trajectory (HYSPLIT) model based on the
227 Global Data Assimilation System (GDAS) to identify the major transport pathways of O_3 (Draxler and
228 Hess, 1998). Moreover, the calculated backward trajectories were clustered into three groups using
229 Ward's variance method and Angle Distance algorithm (Ward 1963; Wang et al., 2006).

230 In order to determine the potential source locations of O_3 over CAS (NAMORS), the Potential Source
231 Contribution Function (PSCF) model and Concentration Weighted Trajectory (CWT) model were used
232 (Hong et al., 2019; Ou et al., 2021). The PSCF was calculated through the number of air trajectory
233 endpoints being divided by the number of air trajectory endpoints. Moreover, a weighting function was
234 introduced to reduce the increased uncertainties of PSCF with the increase of the distance between the
235 grid and sampling point. In this study, the set of this weighting function referred to Yin et al. (2017).
236 CWT can be used to calculate the weight concentration through averaging the concentrations
237 associated with trajectories crossing the grid cell. Above weighting function was also introduced to
238 calculate the WCWT (Hsu, et al., 2003). The detailed description of these two models can be found in
239 Wang et al., 2006.

2.5 Ancillary data

241 The surface NO_2, HONO and O_3 concentrations used to validate the corresponding MAX-DOAS
242 measurements were monitored by broadband cavity enhanced spectrometer (BBCES) (Fang et al.,
243 2017), long path absorption photometer (LOPAP) (Kleffmann et al., 2008) and Thermo Electron 49i
244 (Shi et al., 2009), respectively. The PBL height was simulated using WRF with spatiotemporal
245 resolutions of 20×20 km^2 and 1.0 hour (detailed configurations in Sect. S3 of the supplement).
246 Moreover, the large-scaled spatial distributions of AOD, O_3 and NO_2 over CAS (NAMORS) were
247 monitored by Himawari-8 (Bessho et al., 2016), OMI (Veefkind et al., 2004) and TROPOMI (Griffin et
248 al., 2018; Su et al., 2020), respectively.

3 Results

3.1 Overview of the measurements

251 Figure 3 showed the averaged diurnal variation of AOD from 1st May to 9th July 2019, with an average
252 value of 0.076 km^{-1} during 08:00-19:00. The AOD was 0.071 km^{-1} at 08:00, and then gradually
253 decreased to a minimum value of 0.052 km^{-1} at 12:00. Subsequently, the AOD increased significantly,

reaching maximum values during 15:00-17:00 (average of 0.107km^{-1}), which was about 1.408 times the diurnal average value. Considering the diurnal variation of wind speed (Figure S3), such an enhancement of AOD may be related to the long-range transport of aerosol from southern Asia (Yang et al., 2020; Bi et al., 2023). Moreover, 15:00-17:00 was the active time of tourists and local residents (i.e. cooking), and these kinds of anthropogenic sources contributed to the atmospheric AOD of NAMORS through short-distance transport (Yin et al., 2017; Zhang et al., 2017). After 17:00, the AODs decreased rapidly to 0.071 km^{-1} at 18:00 and 0.081 km^{-1} at 19:00, respectively.
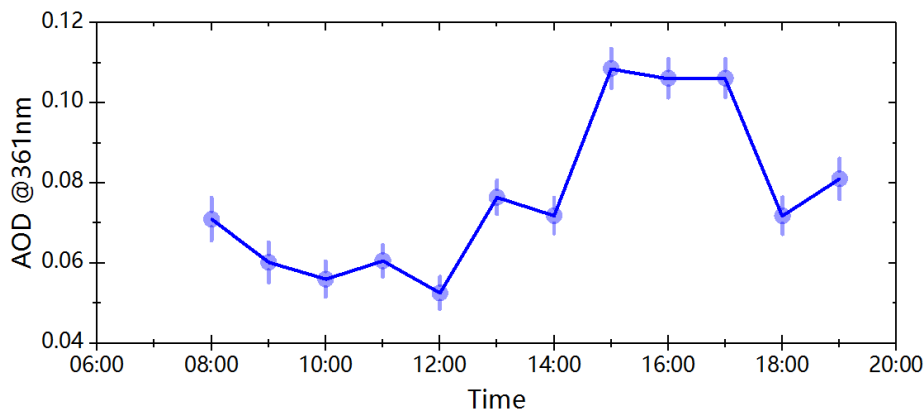
Figure 3. Averaged diurnal variation of AOD at CAS (NAMORS). The error bars represent the mean retrieved errors of AOD.

As shown in Figure S4, the diurnal variation of PBL in Nam Co from May to July 2019 was lower in the early morning and late afternoon, but higher between 11:00 and 17:00, a relatively long period, with the maximum PBL larger than 2.0 km. Zhang et al. (2017) and Yang et al., (2017) also reported that the PBL in Nam Co was usually larger than 1.0 km during daytime in spring and summer. In order to investigate the height-dependent variations of aerosol, H$_2$O, NO$_2$, HONO and O$_3$ within the PBL during the measurements, five height layers under the PBL (0.0-0.2 km, 0.4-0.6 km, 0.8-1.0 km, 1.2-1.4 km and 1.6-1.8 km) were thus selected.

Figure 4 showed the time series of the daily averaged aerosol, H$_2$O, NO$_2$, HONO and O$_3$ at above five layers from 1st May to 9th July 2019. Aerosol mainly distributed at 0.0-0.2 km with an average extinction coefficient of 0.138 km^{-1}, and the ratios of aerosol extinction at 0.4-0.6 km, 0.8-1.0 km, 1.2-1.4 km and 1.6-1.8 km to those at 0.0-0.2 km were 39.34%, 18.77%, 7.29% and 2.62%, respectively. That indicated that the aerosol was usually local-emitted at the surface, and the occasionally appearance of strong aerosol extinction at 0.4-0.6 km, such as 13th and 30th June, was associated with long-range transport from south Asia (Figure S5, Wan et al., 2015; Li et al., 2016). The average concentration of H$_2$O at 0.0-0.2 km was 2.35×10^{17} molec cm^{-3}, and the ratios of H$_2$O at 0.4-0.6 km, 0.8-1.0 km, 1.2-1.4 km and 1.6-1.8 km to those at 0.0-0.2 km were 83.40%, 68.08%, 50.64% and 35.74%, respectively, which should attribute to the transport of H$_2$O from southern Asia driven by the Indian ocean monsoon and the elevated evaporation from Nam Co lake to lead to its not obvious vertical gradient (Figure S6, Lei et al., 2014; Zhu et al., 2019). The average concentration of NO$_2$ at 0.0-0.2 km was 0.193 ppb, and its high concentration mainly distributed at 0.4-0.6 km after 15th May. The ratios of NO$_2$ at 0.4-0.6 km, 0.8-1.0 km, 1.2-1.4 km and 1.6-1.8 km to those at the bottom layer were 104.03%, 59.05%, 24.62% and 12.84%, respectively. The elevation of the distribution height of high concentration NO$_2$ should be attributed to the transport process from the NO$_x$ produced by ice and snow on the top of Mt. Tanggula under strong ultraviolet radiation (Boxe et al., 2005; Fisher 2005; Lin et al., 2021). As depicted in Figure S7, the WPSCF passing through Mt. Tanggula showed high values at 300-400 m layer, especially at 400 m (> 0.3). It also indirectly indicated that the important contribution to NO$_x$ from ice and snow on the top of mountains under strong ultraviolet radiation on the TP. HONO mainly distributed at 0.0-0.2 km with an average value of 0.087 ppb, and the ratios of HONO at 0.4-0.6 km, 0.8-1.0 km, 1.2-1.4 km and 1.6-1.8 km to those at 0.0-0.2 km were 58.49%, 44.64%, 31.30% and 21.67%, respectively. That indicated that the primary and secondary sources of HONO were mainly at the surface (Section 4.2). The vertical gradient of daily averaged O$_3$ concentration was also not obvious, which was associated with its vertical mixing and photochemical

8

production (Yin et al., 2017). As shown in Figure S8, the corresponding TROPOMI O_3 profiles in Nam Co and O_3 profiles measured by lidar and ozonesonde around Nam Co reported in several previous studies also exhibited an exponential shape (Fang et al., 2019; Zhang et al., 2020; Yu et al., 2022). The O_3 average concentration at 0.0-0.2 km was 63.030 ppb, and the ratios of O_3 at 0.4-0.6 km, 0.8-1.0 km, 1.2-1.4 km and 1.6-1.8 km to those at surface were 89.25%, 82.44%, 80.16% and 79.13%, respectively.
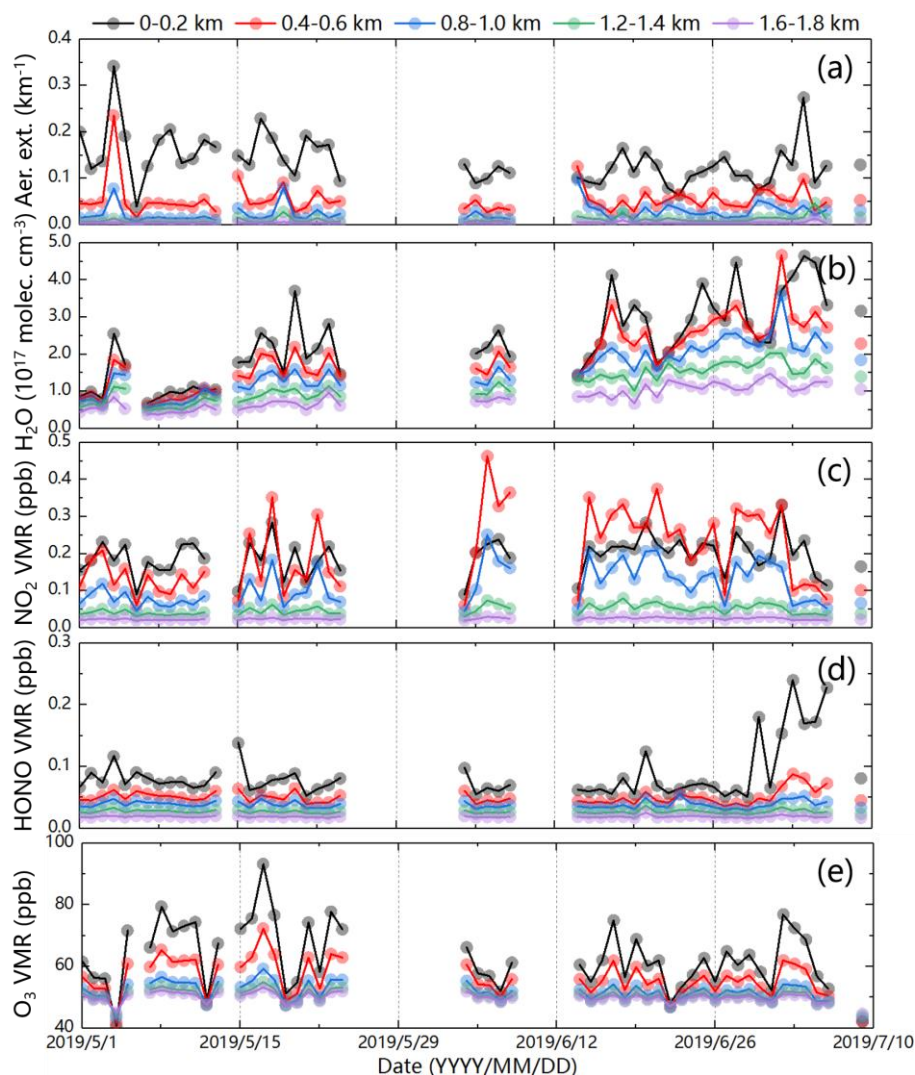
Figure 4. Time series of daily averaged (a) aerosol extinction, (b) H_2O, (c) NO_2, (d) HONO, and (e) O_3 monitored by MAX-DOAS at 0-0.2, 0.4-0.6, 0.8-1.0, 1.2-1.4 and 1.6-1.8 km five height layers from 01 May to 09 July 2019.

3.2 Vertical distributions of aerosol, H_2O, NO_2, HONO and O_3

The first row in Figure 5 provided the averaged vertical profiles of aerosol, H_2O, NO_2, HONO and O_3 from May to July 2019. We found that the vertical profiles of aerosol, H_2O, HONO and O_3 all exhibited an exponential shape with maximum values near the surface, while NO_2 exhibited a Gaussian shape with the maximum value of 0.321 ppb occurring at 0.3-0.4 km layer. In addition to the effect of NO_x transport, Xu et al. (2018) also revealed that the long-range high-altitude transport process from the northern south Asian subcontinent can significantly enhance the Nam Co's peroxyacetyl nitrate (PAN) level which is a reservoir of NO_x. As shown in the second row of Figure 5, the monthly averaged aerosol vertical profiles from May to July 2019 all exhibited an exponential shape, and varied in the order of May (0.17 km^{-1}) > July (0.14 km^{-1}) > June (0.11 km^{-1}). Xu et al. (2018) and Neupane et al. (2019) also reported a similar monthly variations of black carbon (BC) from May to July over the TP, and revealed that it was mainly associated with the anthropogenic emissions (i.e. biomass burning) and its transport from south Asia. The monthly averaged vertical profile of H_2O in May and July exhibited an exponential shape, while its maximum concentration layer slightly elevated to 0.1-0.2 km

9

319 in June which was related to the strongest monsoon transport (Figure S9). It varied in the order of July
320 (3.68×10^{17} molec cm^{-3}) > June (2.71×10^{17} molec cm^{-3}) > May (2.26×10^{17} molec cm^{-3}), and its
321 maximum concentration occurring in July was strongly associated with the enhanced evaporation from
322 the Nam Co lake (Xu et al., 2011). The monthly averaged vertical profiles of NO$_2$ all exhibited a
323 Gaussian shape from May to July, and its maximum values mainly distributed at 0.2-0.4 km layer
324 varying in the order of June (0.39 ppb) > May (0.31 ppb) > July (0.28 ppb). It indicated that the
325 regional transport from the NO$_x$ produced from ice and snow under strong shortwave radiation (Figure
326 S7), NO$_2$ emitted from vehicles due to the increased tourism, anthropogenic emissions from local
327 residents (i.e. biomass burning and religious activities) played an important role in the vertical
328 distribution characteristic of NO$_2$ (Boxe et al., 2005; Chen et al., 2019). The monthly averaged vertical
329 profiles of HONO from May to July all exhibited an exponential shape, with maximum values near the
330 surface varying in the order of July (0.13 ppb) > May (0.07 ppb) > June (0.06 ppb). The local direct
331 emissions from biomass burning, vehicles and soil should be main sources of the surface HONO (Xing
332 et al., 2021). Moreover, the heterogeneous reaction of NO$_2$ on wet surfaces should be another important
333 source of HONO at different height layers (Section 4.2). For example, the aerosol extinction coefficient,
334 and the concentrations of H$_2$O and NO$_2$ were all relatively large at the bottom layer in July,
335 correspondingly, we observed the highest concentration of HONO near the surface in this month. The
336 monthly averaged O$_3$ vertical profiles all showed an exponential shape from May to July, and its
337 surface concentration varied in the order of May (66.71 ppb) > July (61.45 ppb) > June (59.55 ppb).
338 This kind of monthly variation trend of O$_3$ was also reported by several previous studies (Yin et al.,
339 2017; Xu et al., 2018). The O$_3$ in Nam Co was mainly sourced from stratospheric intrusion,
340 photochemical reactions, long-range transport and local vertical mixing (Yin et al., 2017; Chen et al.,
341 2019).
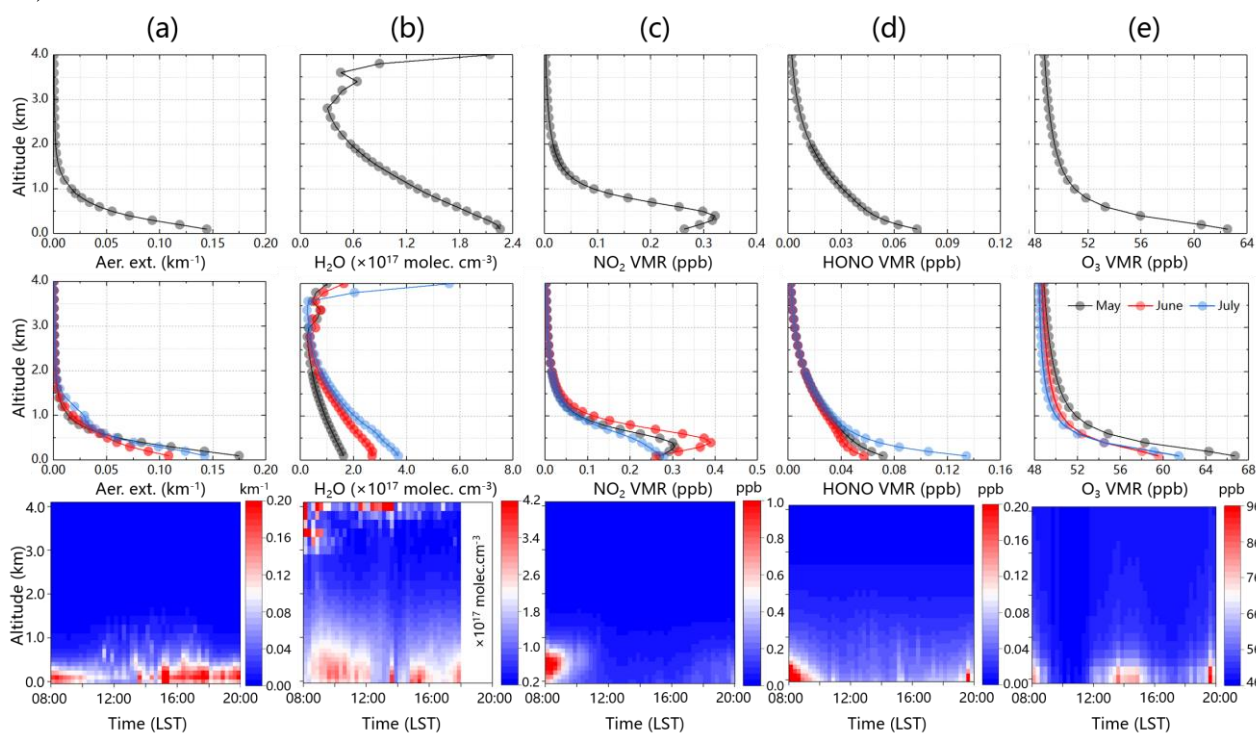
342

343 Figure 5. Vertical profiles of (a) aerosol extinction, (b) H$_2$O, (c) NO$_2$, (d) HONO, and (e) O$_3$. The top
344 row shows the averaged vertical profiles from 01 May to 09 July 2019. The middle row shows the
345 monthly averaged vertical profiles. The bottom row shows the averaged diurnal vertical profiles from
346 01 May to 09 July 2019.

347 The third row in Figure 5 illustrated the averaged diurnal variations in vertical profiles of aerosol, H$_2$O,
348 NO$_2$, HONO and O$_3$ from May to July 2019. Aerosol mainly distributed under 1.0 km, especially 0.6
349 km, and its mixing height was gradually increased with the rise of the PBL height after 12:00.
350 Moreover, the diurnal variation of aerosol showed a bi-peak pattern, which was in line with the
351 investigation reported by Pokharel et al. (2019). The first peak occurred between 08:00-10:00, and

10

another appeared after 15:00. The first peak should be attributed to the local emission of aerosol and the diurnal cycle of PBL (Zhang et al., 2017; Pokharel et al., 2019). The second peak was driven by regional transport and the interaction between local sandy silt loam surface and local meteorology. The high wind speed (> 4.5 m/s) at surface appeared after 15:00, which coincided with the appearance of the second aerosol peak (Figure S3). Moreover, the high extinction during the second peak was extended to 1.0 km associated with the wind speed larger than 8 m/s (Figure S10), which created a favorable condition for high-altitude aerosol transport. H_2O mainly distributed under 1.0 km and above 3.0 km, and its diurnal variation exhibited a multi-peak pattern. The first peak appeared between 08:00-12:00, which was mainly affected by the monsoon driven long-range transport of H_2O (Cong et al., 2009; Xu et al., 2020). The second and third peaks occurred at 15:00-16:00 and after 17:00, respectively. In addition to long-range transport, the enhanced evaporation from the Nam Co lake also significantly contributed to the appearance of these two peaks of H_2O (Xu et al., 2011). NO_2 mainly distributed at 0.2-0.4 km, and peaked before 10:00 and after 18:00 which were dominated by the effects of local emissions and regional transport from the NO_x formed through ice and snow on the top of Mt. Tanggula under strong ultraviolet radiation (Figure S7) (Boxe et al., 2005; Fisher 2005; Chen et al., 2019; Lin et al., 2021). Moreover, its diurnal mixing height was obviously correlated to the diurnal evolution of PBL height. HONO mainly distributed under 1.0 km, especially 0.4 km. Its diurnal variation showed a multi-peak pattern with three obvious peaks before 10:00, 15:00-16:00, and after 19:00. In addition to local emissions (i.e. vehicle emission, biomass burning and soil emission), the heterogeneous reaction of NO_2 on wet surfaces should be also an important HONO source (Xing et al., 2021). We found that there were larger aerosol extinction (> 0.12 km^{-1}) and higher concentrations of NO_2 (> 0.20 ppb) and H_2O (> 2.27×10^{17} molec cm^{-3}) around three HONO peaks. O_3 mainly distributed under 0.4 km, and its diurnal variation exhibited a multi-peak pattern with three peaks appearing before 09:00, 13:00-15:00 and after 19:00. The appearance of O_3 peaks was mainly associated with the influence of the complex topography of the TP, long-range transport, local vertical mixing and stratospheric intrusion (Yin et al., 2017; Chen et al., 2019; Qian et al., 2022). The active photochemical reaction should be another important source of O_3, especially for its second peak at 13:00-15:00.

3.3 Validation with independent data

In order to validate the MAX-DOAS dataset, we extracted the concentrations of NO_2, HONO and O_3 at the bottom layer (0.0-0.1 km) from their corresponding vertical profiles to compare with in situ measurements. As shown in Figure 6(a-c), we found good agreements between MAX-DOAS and in situ observations with Pearson correlation coefficients (R) of 0.91, 0.62 and 0.82 (regression slope of 0.89, 1.05 and 0.82) for NO_2, HONO and O_3, respectively. That indicated the good reliability of trace gases from MAX-DOAS retrievals. Moreover, we also compared the MAX-DOAS PBL and WRF PBL, and a similar variation trend was found. However, WRF PBL showed a significantly difference in height values with MAX-DOAS PBL before 12:00. That should be due to the simulation uncertainties for WRF model at Tibetan plateau with complex topography and meteorology (Yang et al., 2016; Xu et al., 2019).
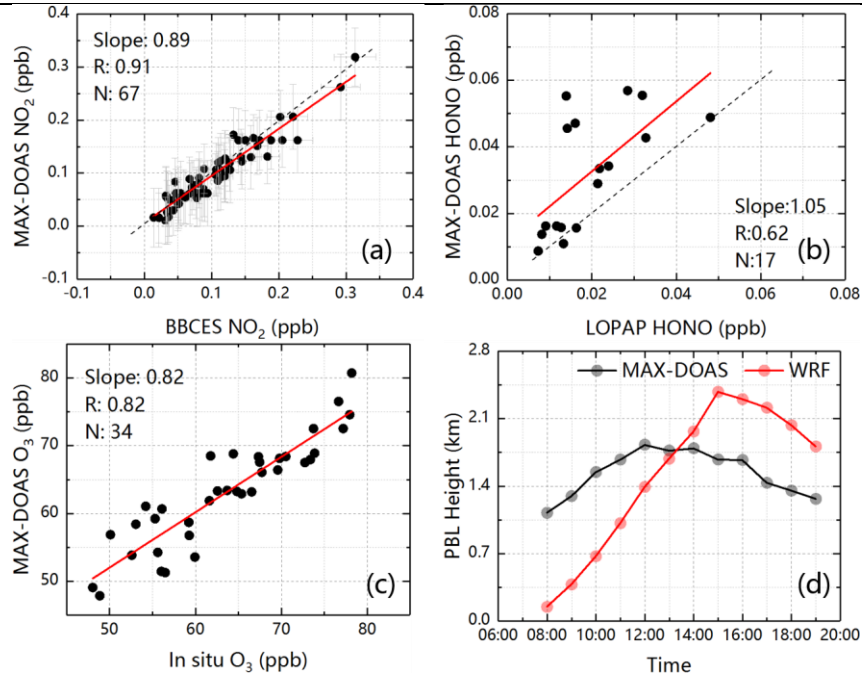
Figure 6. Validations of (a) MAX-DOAS NO_2 vs in situ NO_2 (error bars represent the retrieved errors of NO_2 from MAX-DOAS and BBCES), (b) MAX-DOAS HONO vs LOPAP HONO, (c) MAX-DOAS O_3 vs in situ O_3, and (d) MAX-DOAS PBL vs WRF PBL.

4 Discussion

4.1 OH production

HONO and O_3 are two important precursors of OH redical to enhance the AOC (Kleffmann et al., 2005; Ryan et al., 2018; Xing et al., 2021). In order to evaluate the AOC on the TP, we tried to analyze the OH production from HONO and O_3 at different height layers through vertical observations and TUV calculations. The OH production rates from HONO and O_3 were calculated using the following two equations:

$$P(OH)_{HONO} = J(HONO) \times [HONO]$$

$$P(OH)_{O_3} = 2 \times f \times J(O(^1D)) \times [O_3]$$

Where $J(HONO)$ and $J(O(^1D))$ were the photolysis rates of HONO and $O(^1D)$ calculated using TUV model. $O(^1D)$ was the product from O_3 photolysis by UV radiation. f was the fraction of the process $O(^1D) + H_2O \rightarrow 2OH$.

Figure 7(a-b) showed the averaged diurnal vertical distributions of the photolysis rates $J(HONO)$ and $J(O(^1D))$ from May to July 2019. We found that the maximum $J(HONO)$ and $J(O(^1D))$ were all appeared at the bottom layer between 12:30 and 15:30 with values of 2.0×10^{-3} and 6.75×10^{-5} s^{-1}, respectively. The maximum values were usually larger than that at low-altitude areas due to the stronger solar UV radiation on the TP (Su et al., 2008; Xing et al., 2021; Yang et al., 2021; Liu et al., 2022), but being consistent with the values on the TP reported by Lin et al. (2008). Moreover, it should be noted that the values of $J(HONO)$ and $J(O(^1D))$ all decreased with the increase of altitude, which was significantly different with previous studies in low altitudes (Ryan et al., 2018; Xing et al., 2021; Xu et al., 2021).

12
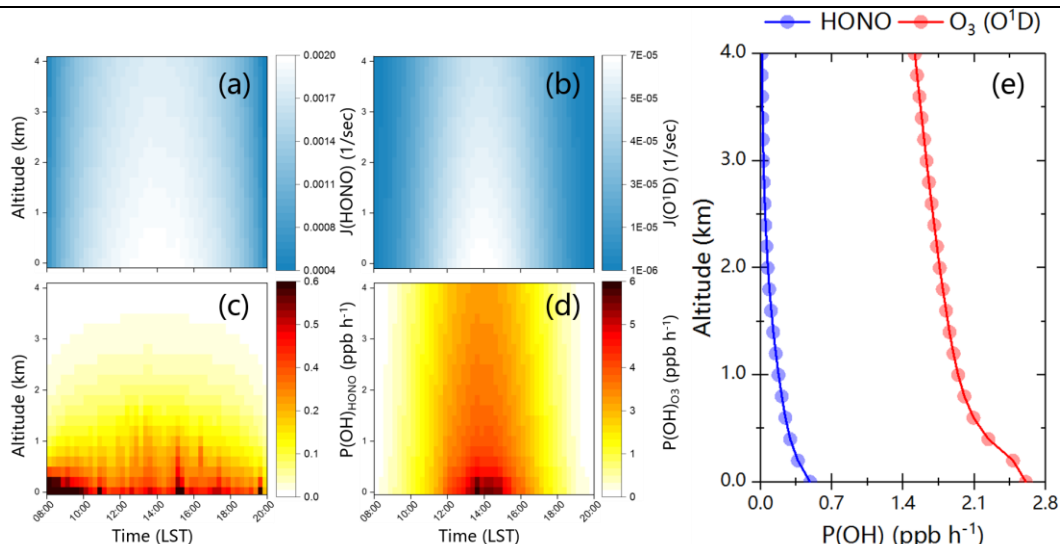
Figure 7. Averaged diurnal vertical profiles of the (a) photolysis rate *J(HONO)*, (b) photolysis rate *J(O(^{1}D))*, (c) OH radical production rates from HONO photolysis, (d) OH radical production rates from O$_3$ photolysis. (e) shows the averaged vertical profiles of OH radical production rates from HONO and O$_3$ photolysis from 01 May to 09 July 2019.

Figure 7(c-d) showed the averaged diurnal vertical profiles of OH production rates from HONO and O$_3$ photolysis from May to July 2019. P(OH)$_{HONO}$ exhibited a multi-peak pattern which mainly appeared before 10:00, 15:00-16:00, and after 19:00 at 0-0.4 km with a maximum value of 0.81 ppb/h. While P(OH)O$_3$ showed a unimodal pattern occurring at 13:00-15:00 under 0.4 km with a maximum value of 6.20 ppb/h. The averaged vertical profiles of P(OH)$_{HONO}$ and P(OH)$_{O3}$ during the observation were depicted in Figure 7(e). We found that the maximum values of P(OH)$_{HONO}$ (0.49 ppb/h) and P(OH)$_{O3}$ (2.61 ppb/h) all appeared at the bottom layer, and decreased with height. That indicated O$_3$ was the main contributor of OH production (> 80%) on the TP, which was about 5-6 times to HONO. Moreover, the OH production rates from HONO and O$_3$ in other cities of China were depicted in Table 3. The contribution percentage of O$_3$ to P(OH) in Nam Co was significantly higher than that in other cities, which was due to the relatively high concentrations of O$_3$ and H$_2$O, and the strong radiation in Nam Co. In addition, P(OH)$_{HONO}$ in Nam Co was close to that in relatively dry areas (i.e. Beijing and Xianghe), but slightly lower than that in areas with relatively high humidity which can enhance the heterogeneous production of HONO (Ryan et al., 2018; Liu et al., 2019; Xing et al., 2021).

Table 3. The maximum OH production rates contributed from HONO and O$_3$ at different locations.

Location	Date	*P(OH)$_{HONO}$* (ppb/h)	*P(OH)$_{O3}$* (ppb/h)	References
Xianghe (China)	Jul. 2008-Apr. 2009	~0.80 in Spring ~0.70 in Summer	~0.20 in Spring, ~0.45 in Summer	Hendrick et al. (2014)
Beijing (China)	Mar. 2010-Dec. 2012	~1.25 in Spring, ~0.70 in Summer	~0.10 in Spring, ~0.55 in Summer	Hendrick et al. (2014)
East China Sea (China)	Jun. 2017	~1.75	~1.20	Cui et al. (2019)
Chengdu (China)	Aug.-Sep. 2019	~3.25	-	Yang et al. (2021)
Qingdao (China)	Jul.-Aug. 2019	~1.30	~1.00	Yang et al. (2021)
Nam Co (China)	May-Jul. 2019	0.81	6.20	This study

4.2 Possible daytime HONO sources

Atmospheric HONO mainly sourced from direct emission, homogeneous reaction and heterogeneous reaction (Fu et al., 2019; Ren et al., 2020; Chai et al., 2021; Crilley et al., 2021; Li et al., 2021). There were less anthropogenic emissions for HONO around NAMORS, however, the open burning of crop residues and soil emissions should be important HONO sources considering the pasture environment and large amounts of animal manure (Cui et al., 2021a; 2021b). Moreover, the background of low-level NO on the TP leaded to the homogeneous reaction not to be the main source of HONO at NAMORS (Lin et al., 2019; Xing et al., 2021; Li et al., 2022). Heterogeneous reaction of NO$_2$ on wet surfaces became an important potential source of HONO around NAMORS, which affected by the humidity,

temperature, solar radiation, aerosol concentration and corresponding specific surface area. In order to remove the effect of diurnal PBL evolution, we used $HONO/NO_2$ to indicate the extent of the heterogeneous reaction process. As shown in Figure 8, scatter plots between $HONO/NO_2$ and H_2O were illustrated. We found that the maximum value of $HONO/NO_2$ appeared around water vapor being around 1.0×10^{17} molec cm^{-3} under 1.0 km, and being around 0.5-1.0×10^{17} molec cm^{-3} at 1.0-2.0 km height layer. This phenomenon of $HONO/NO_2$ firstly increasing and then decreasing with the increasing of H_2O (or relative humidity) was usually found in low-altitude areas in previous studies (Wang et al., 2013; Liu et al., 2019; Xing et al., 2021; Xu et al., 2021). When the H_2O was greater than above mentioned critical values at different heights, $HONO/NO_2$ gradually decreased, which was related to the efficient uptake of HONO and the decrease of NO_2 reactivity with the increase of H_2O (Liu et al., 2019; Xu et al., 2021). That indicated H_2O has significant enhancement for the conversion rate of NO_2 to HONO. Moreover, we found that the high value areas of $HONO/NO_2$ at above five height layers were all accompanied by high aerosol extinction (> 0.15 km^{-1} under 1.0 km, and > 0.02 km^{-1} at 1.0-2.0 km). It indicated that aerosol surface has contribution to the heterogeneous reaction process of NO_2. The scatter plots between HONO and NO_2 at above five layers (Figure S11) also confirmed the possibility of the NO_2 heterogeneous reaction to generate HONO on the TP, and the contribution of atmospheric H_2O and aerosol extinction to this process.
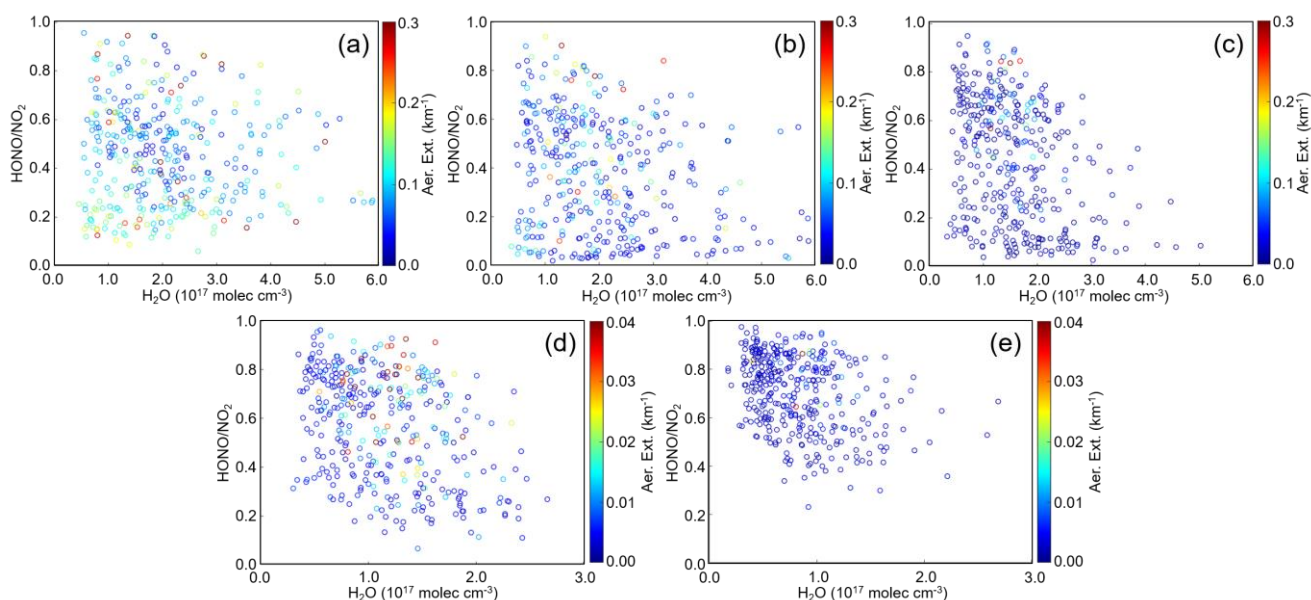
Figure 8. Scatter plots between $HONO/NO_2$ and H_2O colored by aerosol extinction at (a) 0.0-0.2 km, (b) 0.4-0.6 km, (c) 0.8-1.0 km, (d) 1.2-1.4 km, (and e) 1.6-1.8 km from 1st May to 9th July 2019.

In Figure 9, the vertical profile of $HONO/NO_2$ from May to July 2019 was depicted. We found that $HONO/NO_2$ firstly decreased and then increased with the increasing of height, which was opposite to previous studies in low-altitude areas (Meng et al., 2020; Zhang et al., 2020; Xing et al., 2021; Xu et al., 2021). The minimum average $HONO/NO_2$ occurred at 0.3-0.4 km height layer with a value of 0.37. The relatively high values of $HONO/NO_2$ at the bottom layer should be related to the non-deducted HONO direct emissions.
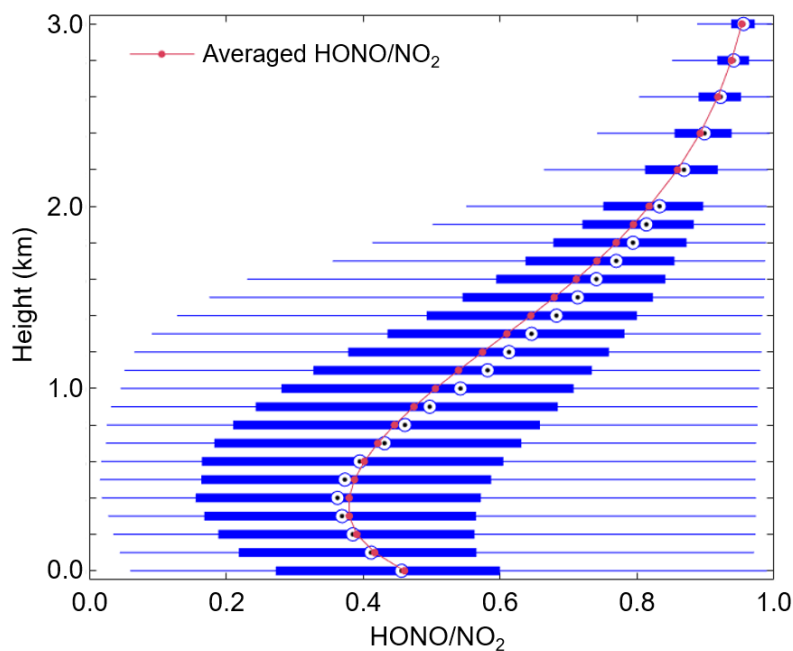
Figure 9. Statistics for the vertical profile of HONO/NO$_2$ from 1st May to 9th July 2019. The left and right of the blue box represent the 25th and 75th percentiles, respectively; the dot within the box represents the mean.

4.3 Possible daytime O$_3$ sources

In addition to local photochemistry process, long-range transport was the main source of O$_3$ on the TP (Yin et al., 2017; Xu et al., 2018). To further understand the transport pathway and potential source of O$_3$, cluster analysis, WPSCF and WCWT models were used to assess the regional representativity of O$_3$ at five typical heights (200 m, 600 m, 1000 m, 1400 m and 1800 m). As shown in Figure S12 and Table 4, the backward trajectories arriving at NAMORS during the observation were classified into three clusters at 200 m, 600 m, 1400 m, 1800 m, and four clusters at 1000 m. We found that cluster 3 was associated with the highest O$_3$ concentration at 200 m (65.48$\pm$17.41 ppb) and 1800 m (49.69$\pm$ 2.21 ppb), and cluster 1 were related to the highest O$_3$ concentration at 600 m (54.67$\pm$6.94 ppb), 1000 m (51.61$\pm$3.84 ppb) and 1400 m (50.51$\pm$2.89 ppb). These two clusters were all originating from northwestern of south Asian subcontinent passing through Himalayas, which was also reported by Yin et al. (2017) during springtime from 2011 to 2015. In Figure S13 and 10, WPSCF and WCWT analysis told us that the high O$_3$ concentration at above heights potentially sourced from northern India, central Pakistan, Nepal, western Bhutan and northern Bangladesh through long-range transport. It should be noted that the potential contribution to O$_3$ at NAMORS at 200 m from above potential source areas were all over 40 ppb. These contributions from the mentioned potential source areas at other four heights were also over 20-30 ppb. The massive fire emissions during springtime were an important source of O$_3$ in south Asia (Jena et al., 2015), and the obvious burning during the observation was observed in Figure S14. Moreover, the abundant precursors and high photochemical activity were another significant sources of O$_3$ in south Asia (Kumar et al., 2012; Sharma et al., 2017).

In addition, Figure 10 showed that the contribution of O$_3$ transported from Himalayas can even up to 50 ppb, especially under 600 m. Several previous studies have revealed that the stratospheric O$_3$ intrusion events were frequent in the Himalayas during spring and summer (Cristofanelli et al., 2010; Chen et al., 2011; Škerlak et al., 2014; Putero et al., 2016). Therefore, the O$_3$ from stratospheric intrusions in the Himalayas can affect the O$_3$ at NAMORS through long-range transport.

Table 4. Trajectory ratios and averaged O$_3$ concentration for all trajectory clusters arriving in Nam Co at 200 m, 600 m, 1000 m, 1400 m and 1800 m from May to July 2019.

	Cluster	Traj_ratio	O$_3$ concentration (ppb)
			Mean$\pm$SD

200 m	1	55.86%	61.50 ± 18.15
	2	11.85%	54.57 ± 14.67
	3	32.28%	65.48 ± 17.41
	All	100.00%	61.14 ± 17.74
600 m	1	62.55%	54.67 ± 6.94
	2	14.32%	50.43 ± 6.64
	3	23.13%	53.27 ± 7.63
	All	100.00%	53.39 ± 7.26
1000 m	1	49.16%	51.61 ± 3.84
	2	8.81%	49.60 ± 3.99
	3	22.73%	50.72 ± 4.21
	4	19.30%	51.39 ± 4.49
	All	100.00%	50.98 ± 4.30
1400 m	1	80.14%	50.51 ± 2.89
	2	4.95%	49.12 ± 2.73
	3	14.92%	49.44 ± 3.85
	All	100.00%	50.07 ± 3.15
1800 m	1	83.75%	49.68 ± 2.55
	2	0.00%	49.07 ± 2.23
	3	16.25%	49.69 ± 2.21
	All	100.00%	49.59 ± 2.49

502

503
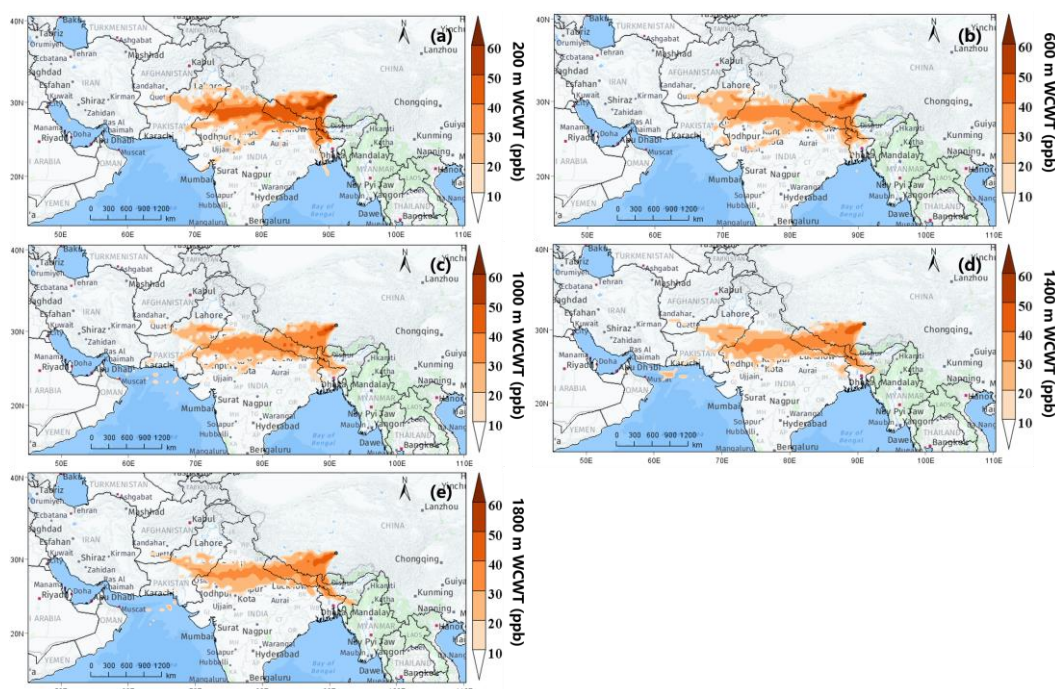
Figure 10. Spatial distributions of WCWT values for O_3 at (a) 200 m, (b) 600 m, (c) 1000 m, (d) 1400 m, and (e) 1800 m height layers from 01st May to 09th July 2019 over CAS (NAMORS).

5 Summary and conclusions

MAX-DOAS measurements were performed to clarify the vertical distributions of several atmospheric components (aerosol, H_2O, NO_2, HONO and O_3), and to explore the AOC in vertical space in Nam Co from May to July 2019. The MAX-DOAS NO_2, HONO and O_3 agreed well with in situ measurements, with correlation coefficients of 0.91, 0.62 and 0.82, respectively. We found that the averaged vertical

16

profiles of aerosol, H$_2$O, HONO and O$_3$ all exhibited an exponential shape, while NO$_2$ showed a Gaussian shape with a maximum value of 0.32 ppb appearing at 300-400 m. The maximum concentrations of monthly averaged aerosol (0.17 km^{-1}) and O$_3$ (66.71 ppb) appeared on May, H$_2$O (3.68$\times$10^{17} molec cm^{-3}) and HONO (0.13 ppb) appeared on July, and NO$_2$ (0.39 ppb) occurred on June. For the diurnal variation, above five species all mainly distributed under 1.0 km, and mostly exhibited a multi-peak pattern considering the effect of regional transport and local chemical reaction.

O$_3$ and HONO were the main source of OH on the TP. The diurnal averaged OH production rate from HONO during the observation exhibited a multi-peak pattern appearing before 10:00, 15:00-16:00 and after 19:00 under 0.4 km with the maximum value of 0.81 ppb/h. The OH production rate from O$_3$ shown a unimodal pattern occurring at 13:00-15:00 under 0.4 km with the maximum value of 6.20 ppb/h which was obviously higher than that at low-altitude areas. In addition to direct emission, the heterogeneous reaction of NO$_2$ on wet surfaces was also an important source of HONO in Nam Co. We found that HONO/NO$_2$ first increasing and then decreasing with the increasing of H$_2$O. The maximum value of HONO/NO$_2$ appeared around H$_2$O being around 1.0$\times$10^{17} molec cm^{-3} under 1.0 km, and being around 1.0-2.0$\times$10^{17} molec cm^{-3} at 1.0-2.0 km height layer. Moreover, high values of HONO/NO$_2$ usually accompanied by high aerosol extinction. O$_3$ under 2.0 km were potentially sourced from Himalayas, northern India, central Pakistan, Nepal, western Bhutan and northern Bangladesh through long-range transport. Our results draw a picture of further understanding the spatial and temporal variations in oxidation chemistry under PBL and provided a new perspective for source analysis of major atmospheric components through vertical observation on the TP.

Acknowledgements

Compliance with ethics guidelines

All authors declare that they have no conflict of interest or financial conflicts to disclose.

References

[1] Kang, S., Chen, P., Li, C., Liu, B., and Cong, Z.: Atmospheric Aerosol Elements over the Inland Tibetan Plateau: Concentration, Seasonality, and Transport, Aerosol Air Qual. Res., 16: 789–800, doi: 10.4209/aaqr.2015.05.0307, 2016.

[2] Xia, X., Zong, X., Cong, Z., Chen, H., Kang, S., and Wang, P.: Baseline continental aerosol over the central Tibetan plateau and a case study of aerosol transport from South Asia, Atmos. Environ., 45, 7370-7378, doi: 10.1016/j.atmosenv.2011.07.067, 2011.

[3] Xing, C., Liu, C., Wang, S., Hu, Q., Liu, H., Tan, W., Zhang, W., Li, B., and Liu, J.: A new method to determine the aerosol optical properties from multiple-wavelength O$_4$ absorption by MAX-DOAS observation, Atmos. Meas. Tech., 12, 3289-3302, doi.org/10.5194/amt-12-3289-2019, 2019.

[4] Zhao, F., Liu, C., Cai, Z., Liu, X., Bak, J., Kim, J., Hu, Q., Xia, C., Zhang, C., Sun, Y., Wang, W., and Liu, J.: Ozone profile retrievals from TROPOMI: Implication for the variation of tropospheric ozone during the outbreak of COVID-19 in China, Sci. Total Environ., 764, 142886, doi.org/10.1016/j.scitotenv.2020.142886, 2021.

[5] Fang, B., Zhao, W., Xu, X., Zhou, J., Ma, X., Wang, S., Zhang, W., Venables, D.S., and Chen, W.: Portable broadband cavity-enhanced spectrometer utilizing Kalman filtering: application to real-time, in situ monitoring of glyoxal and nitrogen dioxide, Opt. Express, 25(22), 26910-26922, doi.org/10.1364/OE.25.026910, 2017.

[6] Kleffmann, J., Wiesen, P.: Technical Note: Quantification of interferences of wet chemical HONO LOPAP measurements under simulated polar conditions, Atmos. Chem. Phys., 8, 6813-6822, doi.org/10.5194/acp-8-6813-2008, 2008.

[7] Bessho, K., Date, K., Hayashi, M., Ikeda, A., Imai, T., Inoue, H., Kumagai, Y., Miyakawa, T., Murata, H., Ohno, T., Okuyama, A., Oyama, R., Sasaki, Y., Shimazu, Y., Shimoji, K., Sumida, Y., Suzuki, M., Taniguchi, H., Tsuchiyama, H., Uesawa, D., Yokota, H., and Yoshida, R.: An Introduction to Himawari-8/9-Japan's New-Generation Geostationary Meteorological Satellites, J. Meteorol. Soc. Jan., 94(2), 151-183, doi: 10.2151/jmsj.2016-009, 2016.

[8] Veefkind, J.P., de Haan, J.F., Brinksma, E.J., Kroon, M., and Levelt, P.F.: Total Ozone From the Ozone Monitoring Instrument (OMI) Using the DOAS Technique, IEEE T. Geosci. Remote Sens., 44(5), 1239-1244, doi: 10.1109/TGRS.2006.871204, 2004.

[9] Griffin, D., Zhao, X., Mclinden, C.A., Boersma, F., Bourassa, A., Dammers, E., Degenstein, D., Eskes, H., Fehr, L., Fioletov, V., Hayden, K., Kharol, S.K., Li, S., Makar, P., Martin, R.V., Mihele, C., Mittermeier, R.L., Krotkov, N., Sneep, M., Lamsal, L.N., ter Linden, M., van Geffen, J., Veefkind, P., and Wolde, M.: High-Resolution Mapping of Nitrogen Dioxide With TROPOMI: First Results and Validation Over the Canadian Oil Sands, Geophys. Res, Lett., 46, 1049-1060, doi: 10.1029/2018GL081095, 2018.

[10] Su, W., Liu, C., Chan, K.L., Hu, Q., Liu, H., Ji, X., Zhu, Y., Liu, T., Zhang, C., Chen, Y., and Liu, J.: An improved TROPOMI tropospheric HCHO retrieval over China, Atmos. Meas. Tech., 13, 6271-6292, doi.org/10.5194/amt-13-6271-2020, 2020.

[11] Grell, G.A., Peckham, S.E., Schmitz, R., McKeen, S.A., Frost, G., Skamarock, W.C., and Eder, B.: Fully coupled "online" chemistry with the WRF model, Atmos, Environ., 39(37), 6957-6975, doi.org/10.1016/j.atmosenv.2005.04.027, 2005.

[12] Shi, G., Yang, L., Wang, Y., Kobayashi, K., Zhu, J., Tang, H., Pan, S., Chen, T., Liu, G., and Wang, Y.: Impact of elevated ozone concentration on yield of four Chinese rice cultivars under fully open-air filed conditions, Agr. Ecosys. Environ., 131(3-4), 178-184, doi.org/10.1016/j.agee.2009.01.009, 2009.

[13] Yin, X., Kang, S., de Foy, B., Cong, Z., Luo, J., Zhang, L., Ma, Y., Zhang, G., Rupakheti, D., and Zhang, Q.: Surface ozone at Nam Co in the inland Tibetan Plateau: variation, synthesis comparison and regional representativeness, Atmos. Chem. Phys., 17, 11293-11311, doi.org/10.5194/acp-17-11293-2017, 2017.

[14] Draxler, R.R., Hess, G.: An overview of the HYSPLIT_4 modelling system for trajectories, Aust. Meteorol. Mag., 47, 295-308, 1998.

[15] Hong, Q., Liu, C., Hu, Q., Xing, C., Tan, W., Liu, H., Huang, Y., Zhu, Y., Zhang, J., Geng, T., and Liu, J.: Evolution of the vertical structure of air pollutants during winter heavy pollution episodes: The role of regional transport and potential sources, Atmos. Res., 228, 106-222, doi.org/10.1016/j.atmosres.2019.05.016, 2019.

[16] Ou, J., Hu, Q., Liu, H., Hong, Q., Xing, C., Tan, W., Lin, H., Wang, X., Xu, H., Zhu, P., and Liu, W.: Vertical characterization and potential sources of aerosols in different seasons over the Yangtze River Delta using ground-based MAX-DOAS, Environ. Pollut., 279, 116898, doi.org/10.1016/j.envpol.2021.116898, 2021.

[17] Hsu, Y.K., Holsen, T.M., Hopke, P.K.: Comparison of hybrid receptor models to locate PCB sources in Chicago, Atmos. Environ., 37, 545-562, doi.org/10.1016/S1352-2310(02)00886-5, 2003.

[18] Wang, Y., Zhang, X., Draxler, R.R.: TrajStat: GIS-based software that uses various trajectory statistical analysis methods to identify potential sources from long-term air pollution measurement data, Environ. Model Softw., 24, 938-939, doi.org/10.1016/j.envsoft.2009.01.004, 2009.

[19] Ye, C.: The first constraint of atmospheric oxidative capacity in Namco, a background Tibetan Plateau research site, AGU Fall Meeting Abstracts, 2019:A51C-08, 2019.

[20] Lin, W., Zhu, T., Song, Y., Zou, H., Tang, M., Tang, X., and Hu, J.: Photolysis of surface O_3 and production potential of OH radicals in the atmosphere over the Tibetan Plateau, J. Geophys. Res.-Atmos., 113, D02309, doi:10.1029/2007JD008831, 2008.

[21] Michoud, V., Kukui, A., Camredon, M., Colomb, A., Borbon, A., Miet, K., Aumont, B., Beekmann, M., Durand-Jolibois, R., Perrier, S., Zapf, P., Siour, G., Ait-Helal, W., Locoge, N., Sauvage, S., Afif, C., Gros, C., Furger, M., Ancellet, G., and Doussin, J.F.: Radical budget analysis in a suburban European site during the MEGAPOLI summer field campaign, Atmos. Chem. Phys., 12, 11951-11974, doi.org/10.5194/acp-12-11951-2012, 2012.

[22] Ryan, R.G., Rhodes, S., Tully, M., Wilson, S., Jones, N., Frieß, U., and Schofield, R.: Daytime HONO, NO_2 and aerosol distributions from MAX-DOAS observations in Melbourne, Atmos. Chem. Phys., 18, 13969-13958, doi.org/10.5194/acp-18-13969-2018, 2018.

[23] Xue, C., Zhang, C., Ye, C., Liu, P., Catoire, V., Krysztofiak, G., Chen, H., Ren, Y., Zhao, X., Wang, J., Zhang, F., Zhang, C., Zhang, J., An, J., Wang, T., Chen, J., Kleffmann, J., Mellouki, A., and Mu, Y.: HONO budget and its role in nitrate formation in rural North China Plain, Environ. Sci. Tech., 54, 18, 11048-11057, doi.org/10.1021/acs.est.0c01832, 2020.

[24] Xing, C., Liu, C., Wu, H., Lin, J., Wang, F., Wang, S., and Gao, M.: Ground-based vertical profile observations of atmospheric composition on the Tibetan Plateau (2017-2019), Earth Syst. Sci. Data, 13, 4897-4912, doi.org/10.5194/essd-13-4897-2021, 2021a.

[25] Xing, C., Liu, C., Hu, Q., Fu, Q., Wang, S., Lin, H., Zhu, Y., Wang, S., Wang, W., Javed, Z., Ji, X., Liu, J.: Vertical distributions of wintertime atmospheric nitrogenous compounds and the corresponding OH radicals production in Leshan, southwest China, J. Environ. Sci., 105, 44-55, doi.org/10.1016/j.jes.2020.11.019.

[26] Luo, S., Holland, F., Rohrer, F., Lu, K., Bohn, B., Brauers, T., Chang, C.C., Fuchs, H., Häseler, R., Kita, K., Kondo, Y., Li, X., Shao, M., Zeng, L., Wahner, A., Zhang, Y., Wang, W., Hofzumahaus, A.: Atmospheric OH

reactivities in the Pearl River Delta-China in summer 2006: measurement and model results, Atmos. Chem. Phys., 10, 11243-11260, doi.org/10.5194/acp-10-11243-2010, 2010.

[27] Yang, Y., Wang, Y., Huang, W., Yao, D., Zhao, S., Wang, Y., Ji, D., Zhang, R., Wang, Y.: Parameterized atmospheric oxidation capacity and speciated OH reactivity over a suburban site in the North China Plain: A comparative study between summer and winter, Sci. Total Environ., 773, 145264, doi.org/10.1016/j.scitotenv.2021.145264, 2021.

[28] Ma, Y., Zhong, L., Su, Z.: Energy and water cycles in the third pole, Water, 14(7), 1175, doi.org/10.3390/w14071175, 2022.

[29] Kang, S., Zhang, Y., Chen, P., Guo, J., Zhang, Q., Cong, Z., Kaspari, S., Tripathee, L., Gao, T., Niu, H., Zhong, X., Chen, X., Hu, Z., Li, X., Li, Y., Neupane, B., Yan, F., Rupakheti, D., Gul, C., Zhang, W., Wu, G., Yang, L., Wang, Z., Li, C.: Black carbon and organic carbon dataset over the Third Pole, Earth Syst. Sci. Data, 14, 683–707, doi.org/10.5194/essd-14-683-2022, 2022.

[30] Ma, Y., Hu, Z., Xie, Z., Ma, W., Wang, B., Chen, X., Li, M., Zhong, L., Sun, F., Gu, L., Han, C., Zhang, L., Liu, X., Ding, Z., Sun, G., Wang, S., Wang, Y., and Wang, Z.: A long-term (2005–2016) dataset of integrated land-atmosphere interaction observations on the Tibetan Plateau, Earth Syst. Sci. Data, 12, 2937-2957, doi:10.5194/essd-12-2937-2020, 2020.

[31] Qu, B., Zhang, Y., Kang, S., Sillanpää, M.: Water quality in the Tibetan Plateau: Major ions and trace elements in rivers of the "Water Tower of Asia", Sci. Total Environ., 649, 571-581, doi.org/10.1016/j.scitotenv.2018.08.316, 2019.

[32] Zhou, S., Sun, F., Wang, M., Zhou, S., and Qing, Y.: Effects of atmospheric heat source on the Tibetan Plateau vortex in different stages: A case study in June 2016, Atmosphere, 13(5), 689, doi:10.3390/atmos13050689, 2022.

[33] Liu, J., Guan, X., Gao, Z., Huang, X., Ma, J., He, Y., and Xie, T.: Inter-decadal variability of the heat source over the Tibetan Plateau, Clim. Dynam., 58, 729-739, doi.org/10.1007/s00382-021-05929-z, 2022.

[34] Chen, P., Kang, S., Bai, J., Sillanpää, M., Li, C.: Yak dung combustion aerosols in the Tibetan Plateau: Chemical characteristics and influence on the local atmospheric environment, Atmos. Res., 156, 58-66, doi.org/10.1016/j.atmosres.2015.01.001, 2015.

[35] Boos, W. R. and Kuang, Z.: Dominant control of the South Asian monsoon by orographic insulation versus plateau heating, Nature, 463, 218–222, doi:10.1038/nature08707, 2010.

[36] Yanai, M., Li, C., and Song, Z.: Seasonal Heating of the Tibetan Plateau and Its Effects on the Evolution of the Asian Summer Monsoon, J. Meteorol. Soc. Jpn. Ser. II, 70, 319–351, doi:10.2151/jmsj1965.70.1B_319, 1992.

[37] Li, C., Zou, Q., Xu, X., and Gao, S.: Water vapor transport around the Tibetan Plateau and its effect on summer rainfall over the Yangtze River valley, J. Meteorol. Res., 30, 472-482, doi: 10.1007/s13351-016-5123-1, 2016.

[38] Lei, Y., Zhu, Y., Wang, B., Yao, T., Yang, K., Zhang, X., Zhai, J., and Ma, N.: Extreme lake level changes in the Tibetan Plateau associated with the 2015/2016 El Niño, Geophys. Res. Lett., 46, 11, 5889-5898, doi.org/10.1029/2019GL081946, 2019.

[39] Hsu, H-H., and Liu, X.: Relationship between the Tibetan Plateau heating and East Asian summer monsoon rainfall, Geophys. Res. Lett., 30, 20, doi.org/10.1029/2003GL017909, 2003.

[40] Zhang, L., Guo, X., Zhao, T., Gong, S., Xu, X., Li, Y., Luo, L., Gui, K., Wang, H., Zheng, Y., and Yin, X.: A modelling study of the terrain effects on the haze pollution in Sichuan Basin, Atmos. Environ., 196, 77-85, doi.org/10.1016/j.atmosenv.2018.10.007, 2019.

[41] Barnett, T. P., Adam, J. C., and Lettenmaier, D. P.: Potential impacts of a warming climate on water availability in snow-dominated regions, Nature, 438, 303–309, doi:10.1038/nature04141, 2005.

[42] Bolch, T., Kulkarni, A., Kaab, A., Huggel, C., Paul, F., Cogley, J. G., Frey, H., Kargel, J. S., Fujita, K., Scheel, M., Bajracharya, S., and Stoffel, M.: The State and Fate of Himalayan Glaciers, Science, 336, 310–314, doi:10.1126/science.1215828, 2012.

[43] Cong, Z., Kang, S., Kawamura, K., Liu, B., Wan, X., Wang, Z., Gao, S., and Fu, P.: Carbonaceous aerosols on the south edge of the Tibetan Plateau: concentrations, seasonality and sources, Atmos. Chem. Phys., 15, 1573–1584, https://doi.org/10.5194/acp-15-1573-2015, 2015.

[44] Kang, S. C., Huang, J., Wang, F. Y., Zhang, Q. G., Zhang, Y. L., Li, C. L., Wang, L., Chen, P. F., Sharma, C. M., Li, Q., Sillanpaa, M., Hou, J. Z., Xu, B. Q., and Guo, J. M.: Atmospheric Mercury Depositional Chronology Reconstructed from Lake Sediments and Ice Core in the Himalayas and Tibetan Plateau, Environ. Sci. Technol., 50, 2859–2869, doi:10.1021/acs.est.5b04172, 2016.

[45] Ran, L., Deng, Z., Wu, Y., Li, J., Bai, Z., Lu, Y., Zhuoga, D., and Bian J.: Measurement report: Vertical profiling of particle size distributions over Lhasa, Tibet – tethered balloon-based in situ measurements and source apportionment, Atmos. Chem. Phys., 22, 6217–6229, doi.org/10.5194/acp-22-6217-2022, 2022.

[46] Wang, K., Hattori, S., Lin, M., Ishino, S., Alexander, B., Kamezaki, K., Yoshida, N., and Kang, S.: Isotopic constraints on atmospheric sulfate formation pathways in the Mt. Everest region, southern Tibetan Plateau, Atmos. Chem. Phys., 21, 8357–8376, https://doi.org/10.5194/acp-21-8357-2021, 2021.

[47] Che, J. and Zhao, P.: Characteristics of the summer atmospheric boundary layer height over the Tibetan Plateau and influential factors, Atmos. Chem. Phys., 21, 5253–5268, https://doi.org/10.5194/acp-21-5253-2021, 2021.

[48] Sun, Y., Yin, H., Cheng, Y., Zhang, Q., Zheng, B., Notholt, J., Lu, X., Liu, C., Tian, Y., Liu, J.: Quantifying variability, source, and transport of CO in the urban areas over the Himalayas and Tibetan Plateau, Atmos. Chem. Phys., 21, 9201–9222, https://doi.org/10.5194/acp-21-9201-2021, 2021.

[49] Li, R., Zhao, Y., Zhou, W., Meng, Y., Zhang, Z., and Fu, H.: Developing a novel hybrid model for the estimation of surface 8-h ozone (O_3) across the remote Tibetan Plateau during 2005-2018, Atmos. Chem. Phys., 20, 6159–6175, https://doi.org/10.5194/acp-20-6159-2020.

[50] Gao, M., Gao, J., Zhu, B., Kumar, R., Lu, X., Song, S., Zhang, Y., Jia, B., Wang, P., Beig, G., Hu, J., Ying, Q., Zhang, H., Sherman, P., and McElroy, M. B.: Ozone pollution over China and India: seasonality and sources, Atmos. Chem. Phys., 20, 4399–4414, https://doi.org/10.5194/acp-20-4399-2020, 2020.

[51] Rawat, P., and Naja, M.: Remote sensing study of ozone, NO_2, and CO: some contrary effects of SARS-CoV-2 lockdown over India, Environ. Sci. Pollut. Res., 29, 22515-22530, doi:10.1007/s11356-021-17441-2, 2022.

[52] Huang, J., Minnis, P., Yi, Y., Tang, Q., Wang, X., Hu, Y., Liu, Z., Ayers, K., Trepte, C., and Winker, D.: Summer dust aerosols detected from CALIPSO over the Tibetan Plateau, Geophys. Res. Lett., 34, L18805, https://doi.org/10.1029/2007GL029938, 2007.

[53] Li, R., Zhao, Y., Zhou, W., Meng, Y., Zhang, Z., and Fu, H.: Developing a novel hybrid model for the estimation of surface 8 h ozone (O3) across the remote Tibetan Plateau during 2005–2018, Atmos. Chem. Phys., 20, 6159–6175, https://doi.org/10.5194/acp-20-6159-2020, 2020.

[54] Zhu, J., Xia, X., Che, H., Wang, J., Cong, Z., Zhao, T., Kang, S., Zhang, X., Yu, X., and Zhang, Y.: Spatiotemporal variation of aerosol and potential long-range transport impact over the Tibetan Plateau, China, Atmos. Chem. Phys., 19, 14637–14656, https://doi.org/10.5194/acp-19-14637-2019, 2019.

[55] Xu, X., Sun, C., Chen, D., Zhao, T., Xu, J., Zhang, S., Li, J., Chen, B., Zhao, Y., Xu, H., Dong, L., Sun, X., and Zhu, Y.: A vertical transport window of water vapor in the troposphere over the Tibetan Plateau with implications for global climate change, Atmos. Chem. Phys., 22, 1149–1157, https://doi.org/10.5194/acp-22-1149-2022, 2022.

[56] Xu, X., Wu, H., Yang, X., and Xie, L.: Distribution and transport characteristics of dust aerosol over Tibetan Plateau and Taklimakan Desert in China using MERRA-2 and CALIPSO data, Atmos. Environ., 237, 117670, https://doi.org/10.1016/j.atmosenv.2020.117670, 2020.

[57] Yang, K., Koike, T., and Yang, D.: Surface flux parameterization in the Tibetan Plateau, Bound.-Lay. Meteorol., 106, 245–262, doi:10.1023/A:1021152407334, 2003.

[58] Seidel, D. J., Ao, C. O., and Li, K.: Estimating climatological planetary boundary layer heights from radiosonde observations: Comparison of methods and uncertainty analysis, J. Geophys. Res., 115, D16113, https://doi.org/10.1029/2009JD013680, 2010.

[59] Dong, Q., Huang, Z., Li, W., Li, Z., Song, X., Liu, W., Wang, T., Bi, J., and Shi, J.: Polarization lidar measurements of dust optical properties at the junction of the Taklimakan Desert-Tibetan Plateau, Remote Sens., 14(3), 558, https://doi.org/10.3390/rs14030558, 2022.

[60] Zhang, J., Xia, X., and Wu, X.: First in situ UV profile across the UTLS accompanied by ozone measurement over the Tibetan Plateau, J. Environ., Sci., 98, 71–76, doi:10.1016/j.jes.2020.05.020, 2020.

[61] Fang, X., Li, T., Ban, C., Wu, Z., Li, J., Li, F., Cen, Y., and Tian, B.: A mobile differential absorption lidar for simultaneous observations of tropospheric and stratospheric ozone over Tibet, Opt. Express, 27, 4126–4139, doi:10.1364.OE.27.004126, 2019.

[62] Wang, Y., Pukite, J., Wagner, T., Donner, S.; Beirle, S., Hilboll, A., Vrekoussis, M., Richter, A., Apituley, A., Piters, A., Allaart, M., Eskes, H., Frumau, A., van Roozendael, M., Lampel, J., Platt, U., Schmitt, S., Swart, D., and Vonk, J.: Vertical profles of tropospheric ozone from MAX-DOAS measurement during the CINDI-2 campaign: part 1—Development of a new retrieval algorithm. J. Geophys. Res. Atmos. 123 (18), 10–637. https://doi.org/10.1029/2018JD028647, 2018.

[63] Xing, C., Liu, C., Wang, S., Chan, K.L., Gao, Y., Huang, X., Su, W., Zhang, C., Dong, Y., Fan, G., Zhang, T., Chen, Z., Hu, Q., Su, H., Xie, Z., and Liu, J.: Observations of the vertical distributions of summertime atmospheric pollutants and the corresponding ozone production in Shanghai, China. Atmos. Chem. Phys. 17, 14275–14289. https://doi.org/10.5194/acp-17-14275-2017, 2017.

[64] Xing, C., Liu, C., Wang, S., Hu, Q., Liu, H., Tan, W., Zhang, W., Li, B., and Liu, J.; A new method to determine the aerosol optical properties from multiple-wavelength O4 absorptions by MAX-DOAS observation. Atmos. Meas. Tech. 12, 3289–3302. https://doi.org/10.5194/amt-12-3289-2019, 2019.

[65] Xing, C., Liu, C., Hu, Q., Fu, Q., Lin, H., Wang, S., Su, W., Wang, W., Javed, Z., and Liu, J.: Identifying the wintertime sources of volatile organic compounds (VOCs) from MAX-DOAS measured formaldehyde and glyoxal in Chongqing, Southwest China. Sci. Total Environ. 715, 136258 https://doi.org/10.1016/j.scitotenv.2019.136258, 2020.

[66] Ye, D. Z., and Gao, Y. X.: The Meteorology of the Tibetan Plateau (in Chinese), 278pp., Science Press, Beijing, pp. 39– 48, 1979.

[67] Liu, Y., and Li, W.: Deepening of the ozone valley over Tibetan Plateau and its possible influences (Chinese with English abstract), Acta Meteorologica Sinica, 59(1), 97– 106, 2001.

[68] Yang, J., Kang, S., Hu, Y., Chen, X., Rai, M.: Influence of South Asian biomass burning on ozone and aerosol concentrations over the Tibetan Plateau, Adv. Atmos. Sci., 39, 1184-1197, doi:10.1007/s00376-022-1197-0, 2022.

[69] Yu, J., Meng, L., Chen, Y., Zhang, H., and Liu, J.: Ozone profiles, precursors, and vertical distribution in urban Lhasa, Tibetan Plateau, Remote Sens., 14(11), 2533, https://doi.org/10.3390/rs14112533, 2022.

[70] Li, M., Mao, J., Chen, S., Bian, J., Bai, Z., Wang, X., Chen, W., and Yu, P.: Significant contribution of lightning NO_x to summertime surface O_3 on the Tibetan Plateau, Sci, Total, Environ., 829, 154639, doi.org/10.1016/j.scitotenv.2022.154639, 2022.

[71] Zhou, L., Zhang, X., Zhang, J.: Temporal and spatial distributions of atmospheric hydroxyl radicals based on the observation with the aura microwave limb sounder. Science & Technology Review, 33(17): 69-77, 2015.

[72] Yin, X., Kang, S., de Foy, B., Cong, Z., Luo, J., Zhang, L., Ma, Y., Zhang, G., Rupakheti, D., and Zhang, Q.: Surface ozone at Nam Co in the inland Tibetan Plateau: variation, synthesis comparison and regional representativeness, Atmos. Chem. Phys., 17, 11293–11311, https://doi.org/10.5194/acp-17-11293-2017, 2017.

[73] Xu, X., Zhang, H., Lin, W., Wang, Y., Xu, W., and Jia, S.: First simultaneous measurements of peroxyacetyl nitrate (PAN) and ozone at Nam Co in the central Tibetan Plateau: impacts from the PBL evolution and transport processes, Atmos. Chem. Phys., 18, 5199–5217, https://doi.org/10.5194/acp-18-5199-2018, 2018.

[74] Bi, H., Chen, S., Zhao, D., Lu, F., Chen, Y., and Guan, Y.: Aerosol optical properties and its direct radiative forcing over Tibetan Plateau from 2006 to 2017, Particuology, 74, 64-73, https://doi.org/10.1016/j.partic.2022.05.007, 2023.

[75] Yang, J., Kang, S., and Ji, Z.: Critical contribution of south Asian residential emissions to atmospheric black carbon over the Tibetan plateau, Sci. Total Environ., 709, 135923, https://doi.org/10.1016/j.scitotenv.2019.135923, 2020.

[76] Zhang, X., Ming, J., Li, Z., Wang, F., and Zhang, G.: The online measured black carbon aerosol and source orientations in the Nam Co region, Tibet, Environ. Sci. Pollut. Res., 24, 25021-25033, doi: 10.1007/s11356-017-0165-1, 2017.

[77] Yang, J., Duan, K., Kang, S., Shi, P., and Ji, Z.: Potential feedback between aerosols and meteorological conditions in a heavy pollution event over the Tibetan Plateau and Indo-Gangetic Plain, Clim. Dyn., 48(9), 2901-2917, doi:10.1007/s00382-016-3240-2, 2017.

[78] Wan, X., Kang, S., Wang, Y., Xin, J., Liu, B., Guo, Y., Wen, T., Zhang, G., and Cong, Z.: Size distribution of carbonaceous aerosols at a high-altitude site on the central Tibetan Plateau (Nam Co Station, 4730 m a.s.l.), Atmos. Res, 153, 155-164, doi:10.1016/j.atmosres.2014.08.008, 2015.

[79] Li, C., Bosch, C., Kang, S., Andersson, A., Chen, P., Zhang, Q., Cong, Z., Chen, B., Qin, D., and Gustafsson, O.: Sources of black carbon to the Himalayan-Tibetan Plateau glaciers, Nat. Commun., 7, 12574, doi:10.1038/ncomms12574, 2016.

[80] Lei, Y., Yang, K., Wang, B., Sheng, Y., Bird, B.W., Zhang, G., and Tian, L.: Response of inland lake dynamics over the Tibetan Plateau to climate change, Clim. Chang, 125, 281-290, doi:10.1007/210584-014-1175-3, 2014.

[81] Zhu, G., Guo, H., Qin, D., Pan, H., Jia, W., and Ma, X.: Contribution of recycled moisture to precipitation in the monsoon marginal zone: Estimate based on stable isotope data, J. Hydrol., 569, 423-435, doi:10.1016/j.jhydrol.2018.12.014, 2019.

[82] Boxe, C.: Nitrate photochemistry and interrelated chemical phenomena in ice[M]. California Institute of Technology, 2005.

[83] Xu, R., Tie, X., Li, G., Zhao, S., Cao, J., Feng, T., and Long, X.: Effect of biomass burning on black carbon (BC) in South Asia and Tibetan Plateau: The analysis of WRF-Chem modeling, Sci. Total Environ., 645, 901-912, doi:10.1016/j.scitotenv.2018.07.165, 2018.

[84] Neupane, B., Kang, S., Chen, P., Zhang, Y., Ram, K., Rupakheti, D., Tripathee, L., Sharma, C.M., Cong, Z., Li, C., Hou, J., Xu, M., and Thapa, P.: Historical black carbon reconstruction from the lake sediments of the Himalayan-Tibetan Plateau, Environ. Sci. Tech., 53, 5641-5651, doi:10.1021/acs.est.8b07025, 2019.

[85] Xu, K., Zhong, L., Ma, Y., Zou, M., and Huang, Z.: A study on the water vapor transport trend and water vapor sources of the Tibetan Plateau, Theor. Appl. Climatol., 140, 1031-1042, doi:10.1007/s00704-020-03142-2, 2020.

[86] Xu, Y., Kang, S., Zhang, Y., and Zhang, Y.: A method for estimating the contribution of evaporative vapor from Nam Co to local atmospheric vapor based on stable isotopes of water bodies, Chinese Sci. Bull., 56(14), 1511-1517, doi:10.1007/s11434-011-4467-2, 2011.

[87] Chen, P., Kang, S., Yang, J., Pu, T., Li, C., Guo, J., and Tripathee, L.: Spatial and temporal variations of gaseous and particle pollutants in six sites in Tibet, China, during 2016-2017, Aerosol Air Qual. Res., 19, 516-527, doi:10.4209/aaqr.2018.10.0360, 2019.

[88] Wang, T., Xue, L., Brimblecombe, P., Lam, Y, Li, L. and Zhang, L.: Ozone pollution in China: A review of concentrations, meteorological influences, chemical precursors, and effects. Sci. Total Environ., 575, 1582–1596, doi:10.1016/j.scitotenv.2016.10.081, 2017.

[89] Pokharel, M., Guang, J., Liu, B., Kang, S., Ma, Y., Holben, B.N., Xia, X., Xin, J., Ram, K., Rupakheti, D., Wan, X., Wu, G., Bhattarai, H., Zhao, C., and Cong, Z.: Aerosol properties over Tibetan Plateau from a decade of AERONET measurements: Baseline, types, and influencing factors, J. Geophys. Res.: Atmos., 124, 13357-13374, doi:10.1029/2019JD031293, 2019.

[90] Cong, Z., Kang, S., Smirnov, A., and Holben, B.: Aerosol optical properties at Nam Co, a remote site in central Tibetan Plateau, Atmos. Res, 92, 42-48, doi:10.1016/j.atmosres.2008.08.005, 2009.

[91] Qian, Y., Wang, H., Zhao, C., Zhao, C., Chen, S., Hu, X., and Kang, S.: Understanding third pole atmospheric dynamics and land surface processes and their associations with the cryosphere, air quality, and climate change, Adv. Atmos. Sci., 39, 1017-1020, doi:10.1007/s00376-022-2004-7, 2022.

[92] Xu, L., Liu, H., Du, Q., and Xu, X.: The assessment of the planetary boundary layer schemes in WRF over the central Tibetan Plateau, Atmos. Res., 230, 104644, doi:10.1016/j.atmosres.2019.104644, 2019.

[93] Yang, J., and Duan, K.: Effects of initial drivers and land use on WRF modeling for near-surface fields and atmospheric boundary layer over the northeastern Tibetan Plateau, Adv. Meteorol., 2016, 7849249, doi:10.1155/2016/7849249, 2016.

[94] Kleffmann, J., Gavriloaiei, T., Hofzumahaus, A., Holland, F., Koppmann, R., Rupp, L., Schlosser, E., Siese, M., and Wahner, A.: Daytime formation of nitrous acid: A major source of OH radicals in a forest, Geophys. Res. Lett., 32(5), doi:10.1029/2005GL022524, 2005.

[95] Su, H., Cheng, Y., Shao, M., Gao, D., Yu, Z., Zeng, L., Slanina, J., Zhang, Y., and Wiedensohler, A.: Nitrous acid (HONO) and its daytime sources at a rural site during the 2004 PRIDE-PRD experiment in China, J. Geophys. Res., 113, D14312, doi:10.1029/2007JD009060, 2008.

[96] Yang, Y., Li, X., Zu, K., Lian, C., Chen, S., Dong, H., Feng, M., Liu, H., Liu, J., Lu, K., Lu, S., Ma, X., Song, D., Wang, W., Yang, S., Yang, X., Yu, X., Zhu, Y., Zeng, L., Tan, Q., and Zhang, Y.: Elucidating the effect of HONO and O_3 pollution by a case study in southwest China, Sci. Total Environ., 756, 144127, doi:10.1016/j.scitotenv.2020.144127, 2021.

[97] Liu, T., Hong, Y., Li, M., Xu, L., Chen, J., Bian, Y., Yang, C., Dan, Y., Zhang, Y., Xue, L., Zhao, M., Huang, Z., and Wang, H.: Atmospheric oxidation capacity and ozone pollution mechanism in a coastal city of southeastern China: analysis of a typical photochemical episode by an observation-based model, Atmos. Chem. Phys., 22, 2173-2190, doi:10.5194/acp-22-2173-2022, 2022.

[98] Xu, S., Wang, S., Xia, M., Lin, H., Xing, C., Ji, X., Su, W., Tan, W., Liu, C., and Hu, Q.: Observations by ground-based MAX-DOAS of the vertical characters of winter pollution and the influencing factors of HONO generation in Shanghai, China, Remote Sens., 13, 3518, doi:10.3390/rs13173518, 2021.

[99] Hendrick, F., Müller, J.F., Clémer, K., Wang, P., De Mazière, M., Fayt, C., Gielen, C., Hermans, C., Ma, J., Pinardi, G., Stavrakou, T., Vlemmix, T., Van Roozendael, M.: Four years of ground-based MAX-DOAS observations of HONO and NO2 in the Beijing area, Atmos. Chem. Phys., 14, 765–781, doi:10.5194/acp-14-765-2014, 2014.

[100] Cui, L., Li, R., Fu, H., Li, Q., Zhang, L., George, C., and Chen, J.: Formation features of nitrous acid in the offshore area of the East China Sea, Sci. Total Environ., 682, 138-150, doi: 10.1016/j.scitotenv.2019.05.004, 2019.

[101] Yang, J., Shen, H., Guo, M., Zhao, M., Jiang, Y., Chen, T., Liu, Y., Li, H., Zhu, Y., Meng, H., Wang, W., and Xue, L.: Strong marine-derived nitrous acid (HONO) production observed in the coastal atmosphere of northern China, Atmos. Environ., 244, 117948, doi: 10.1016/j.atmosenv.2020.117948, 2021.

[102] Liu, Y., Nie, W., Xu, Z., Wang, T., Wang, R., Li, Y., Wang, L., Chi, X., and Ding, A.: Semi-quantitative understanding of source contribution to nitrous acid (HONO) based on 1 year of continuous observation at the SORPES station in eastern China, Atmos. Chem. Phys., 19, 13289–13308, doi: 10.5194/acp-19-13289-2019, 2019.

[103] Jena, C., Ghude, S.D., Pfister, G.G., Chate, D.M., Kumar, R., Beig, G., Surendran, D.E., Fadnavis, S., and Lal, D.M.: Influence of springtime biomass burning in South Asia on regional ozone (O3): A model based case study, Atmos. Environ., 100, 37-47, doi:10.1016/j.atmosenv.2014.10.027, 2015.

[104] Xing, L., Bei, N., Guo, J., Wang, Q., Liu, S., Han, Y., Pongpiachan, S., and Li, G.: Impacts of biomass burning in peninsular southeast Asia on $PM_{2.5}$ concentration and ozone formation in southeastern China during springtime-A case study, J. Geophys. Res.: Atmos., 126(22), e2021JD034908, doi:10.1029/2021JD034908, 2021.

[105] Kumar, R., Naja, M., Pfister, G.G., Barth, M.C., Wiedinmyer, C., and Brasseur, G.P.: Simulations over South Asia using the Weather Research and Forecasting model with Chemistry (WRF-Chem): chemistry evaluation and initial results, Geosci. Model Dev., 5, 619–648, doi:10.5194/gmd-5-619-2012, 2012.

[106] Sharma, A., Ojha, N., Pozzer, A., Mar, K.A., Beig, G., Lelieveld, J., and Gunthe, S.S.: WRF-Chem simulated surface ozone over south Asia during the pre-monsoon: effects of emission inventories and chemical mechanisms, Atmos. Chem. Phys., 17, 14393–14413, doi: 10.5194/acp-17-14393-2017, 2017.

[107] Cristofanelli, P., Bracci, A., Sprenger, M., Marinoni, A., Bonafè, U., Calzolari, F., Duchi, R., Laj, P., Pichon, J. M., Roccato, F., Venzac, H., Vuillermoz, E., and Bonasoni, P.: Tropospheric ozone variations at the Nepal Climate ObservatoryPyramid (Himalayas, 5079 m a.s.l.) and influence of deep stratospheric intrusion events, Atmos. Chem. Phys., 10, 6537–6549, doi:10.5194/acp-10-6537-2010, 2010.

[108] Chen, X. L., Ma, Y. M., Kelder, H., Su, Z., and Yang, K.: On the behaviour of the tropopause folding events over the Tibetan Plateau, Atmos. Chem. Phys., 11, 5113–5122, doi:10.5194/acp-11-5113-2011, 2011.

[109] Škerlak, B., Sprenger, M., and Wernli, H.: A global climatology of stratosphere–troposphere exchange using the ERA-Interim data set from 1979 to 2011, Atmos. Chem. Phys., 14, 913–937, doi:10.5194/acp-14-913-2014, 2014.

[110] Putero, D., Cristofanelli, P., Sprenger, M., Škerlak, B., Tositti, L., and Bonasoni, P.: STEFLUX, a tool for investigating stratospheric intrusions: application to two WMO/GAW global stations, Atmos. Chem. Phys., 16, 14203–14217, doi:10.5194/acp-16-14203-2016, 2016.

863 [111] Fu, X., Wang, T., Zhang, L., Li, Q., Wang, Z., Xia, M., Yun, H., Wang, W., Yu, C., Yue, D., Zhou, Y., Zheng,
864 J., and Han, R.: The significant contribution of HONO to secondary pollutants during a severe winter pollution event
865 in southern China, Atmos. Chem. Phys., 19, 1–14, doi: 10.5194/acp-19-1-2019, 2019.

866 [112] Ren, Y., Stieger, B., Spindler, G., Grosselin, B., Mellouki, A., Tuch, T., Wiedensohler, A., and Herrmann, H.:
867 Role of the dew water on the ground surface in HONO distribution: a case measurement in Melpitz, Atmos. Chem.
868 Phys., 20, 13069–13089, doi: 10.5194/acp-20-13069-2020, 2020.

869 [113] Crilley, L.R., Kramer, L.J., Pope, F.D., Reed, C., Lee, J.D., Carpenter, L.J., Hollis, L.D.J., Ball, S.M., and Bloss,
870 W.J.: Is the ocean surface a source of nitrous acid (HONO) in the marine boundary layer? Atmos. Chem. Phys., 21,
871 18213–18225, doi: 10.5194/acp-21-18213-2021, 2021.

872 [114] Li, S., Song, W., Zhan, H., Zhang, Y., Zhang, X., Li, W., Tong, S., Pei, C., Wang, Y., Chen, Y., Huang, Z.,
873 Zhang, R., Zhu, M., Fang, H., Wu, Z., Wang, J., Luo, S., Fu, X., Xiao, S., Huang, X., Zeng, J., Zhang, H., Chen, D.,
874 Gligorovski, S., Ge, M., George, C., and Wang, X.: Contribution of vehicle emission and NO_2 surface conversion to
875 nitrous acid (HONO) in urban environments: Implications from tests in a tunnel, Environ. Sci. Technol., 55(23),
876 15616-15624, doi:10.1021/acs.est.1c00405, 2021.

877 [115] Chai, J., Dibb, J.E., Anderson, B.E., Bekker, C., Blum, D.E., Heim, E., Jordan, C.E., Joyce, E.E., Kaspari, J.H.,
878 Munro, H., Walters, W.W., and Hastings, M.G.: Isotopic evidence for dominant secondary production of HONO in
879 near-ground wildfire plumes, Atmos. Chem. Phys., 21, 13077–13098, doi: 10.5194/acp-21-13077-2021, 2021.

880 [116] Cui, L., and Wang, S.: Mapping the daily nitrous acid (HONO) concentrations across China during 2006-2017
881 through ensemble machine-learning algorithm, Sci. Total Environ., 785, 147325, doi:10.1016/j.scitotenv.2021.147325,
882 2021.

883 [117] Cui, L., Li, R., Fu, H., Meng, Y., Zhao, Y., Li, Q., and Chen, J.: Nitrous acid emission from open burning of
884 major crop residues in mainland China, Atmos. Environ., 244, 117950, doi:10.1016/j.atmosenv.2020.117950, 2021.

885 [118] Su, H., Cheng, Y., Oswald, R., Behrendt, T., Trebs, I., Meixner, F.X., Andreae, M.O., Cheng, P., Zhang, Y., and
886 Poschl, U.: Soil nitrite as a source of atmospheric HONO and OH radicals, Science, 333(6049), 1616-1618,
887 doi:10.1126/science.1207687, 2011.

888 [119] Lin, F., Liu, C., Hu, X., Fu, Y., Zheng, X., Wang, R., Zhang, W., and Cao, G.: Characterizing nitric oxide
889 emissions from two typical alpine ecosystems, J. Environ. Sci., 77, 312-322, doi:10.1016/j.jes.2018.08.011, 2019.

890 [120] Gil, J., Kim, J., Lee, M., Lee, G., Lee, D., Jung, J., An, J., Hong, J., Cho, S., Lee, J., and Long, R.: The role of
891 HONO in O3 formation and insight into its formation mechanism during the KORUS-AQ Campaign, Atmos. Chem.
892 Phys. Disscu., doi: 10.5194/acp-2019-1012, 2019.

893 [121] Wen, L., Chen, T., Zheng, P., Wu, L., Wang, X., Mellouki, A., Xue, L., and Wang, W.: Nitrous acid marine
894 boundary layer over eastern Bohai Sea, China: Characteristics, sources, and implications, Sci. Total Environ., 670,
895 282-291, doi:10.1016/j.scitotenv.2019.03.225, 2019.

896 [122] Lu, X., Wang, Y., Li, J., Shen, L., and Fung, J.C.H.: Evidence of heterogeneous HONO formation from aerosols
897 and the regional photochemical impact of this HONO source, Environ. Res. Lett. 13, 114002,
898 doi:10.1088/1748-9326aae492, 2018.

899 [123] Cui, L., Li, R., Zhang, Y., Meng, Y., Fu, H., and Chen, J.: An observational study of nitrous acid (HONO) in
900 Shanghai, China: The aerosol impact on HONO formation during the haze episodes, Sci. Total Environ., 630,
901 1057-1070, doi:10.1016/j.scitotenv.2018.02.063, 2018.

902 [124] Wang, S., Zhou, R., Zhao, H., Wang, Z., Chen, L., and Zhou, B.: Long-term observation of atmospheric nitrous
903 acid (HONO) and its implication to local NO_2 levels in Shanghai, China, Atmos. Environ., 77, 718–724,
904 doi:10.1016/j.atmosenv.2013.05.071, 2013.

905 [125] Meng, F., Qin, M., Tang, K., Duan, J., Fang, W., Liang, S., Ye, K., Xie, P., Sun, Y., Xie, C., Ye, C., Fu, P., Liu,
906 J., and Liu, W.: High-resolution vertical distribution and sources of HONO and NO_2 in the nocturnal boundary layer
907 in urban Beijing, China, Atmos. Chem. Phys., 20, 5071–5092, doi: 10.5194/acp-20-5071-2020, 2020.

908 [126] Zhang, W., Tong, S., Jia, C., Wang, L., Liu, B., Tang, G., Ji, D., Hu, B., Liu, Z., Li, W., Wang, Z., Liu, Y.,
909 Wang, Y., and Ge, M.: Different HONO sources for three layer at the urban area of Beijing, Environ. Sci. Technol.,
910 54, 12870-12880, doi:10.1021/acs.est.0c02146, 2020.

911 [127] Fang, X., Li, T., Ban, C., Wu, Z., Li, J., Li, F., Cen, Y., and Tian, B.: A mobile differential absorption lidar for
912 simultaneous observations of tropospheric and stratospheric ozone over Tibet, Opt. Express, 27(4), 4126-4139,
913 doi:10.1364/OE.27.004126, 2019.

914 [128] Yu, J., Meng, L., Chen, Y., Zhang, H., and Liu, J.: Ozone profiles, precursors, and vertical distribution in urban
915 Lhasa, Tibetan Plateau, Remote Sens., 14(11), doi:10.3390/rs14112533, 2022.

916 [129] Zhang, J., Xia, X., and Wu, X.: First in situ UV profile across the UTLS accompanied by ozone measurement
917 over the Tibetan Plateau, J. Environ. Sci., 98, 71-76, doi:10.1016/j.jes.2020.05.020.

918 [130] Fisher, F. N.: Extinction of UV-visible radiation in wet midlatitude (maritime) snow: Implications for increased
919 NOx emission, J. Geophys. Res., 110, D21301, doi:10.1029/2005JD005963, 2005.

920 [131] Lin, W., Wang, F., Ye, C., Zhu, T.: Observation of strong NO_x release over Qiyi Glacier, China. The
921 Cryosphere, doi.org/10.5194/tc-2021-32, 2021.

[132] Ji, X., Liu, C., Wang, Y., Hu, Q., Lin, H., Zhao, F., Xing, C., Tang, G., Zhang, J., Wagner, T.: Ozone profiles without blind area retrieved from MAX-DOAS measurements and comprehensive validation with multi-platform observations. Remote Sens. Environ., 284, 113339, doi.org/10.1016/j.res.2022.113339, 2023.

[133] Lin, H., Liu, C., Xing, C., Hu, Q., Hong, Q., Liu, H., Li, Q., Tan, W., Ji, X., Wang, Z., Liu, J.: Validation of water vapor vertical distributions retrieved from MAX-DOAS over Beijing, China. Remote Sens., 12, 3193, doi.org/10.3390/rs12193193, 2020.

[134] Xing, C., Xu, S., Song, Y., Liu, C., Liu, Y., Lu, K., Tan, W., Zhang, C., Hu, Q., Wang, S., Wu, H., Lin, H.: A new insight into the vertical differences in NO_2 heterogeneous reaction to produce HONO over inland and marginal seas. Atmos. Chem. Phys., 23, 5815-5834, doi.org/10.5194/acp-23-5815-2023, 2023.

[135] Rodgers, C. D.: Inverse methods for atmospheric sounding: theory and practice. Singapore-New Jersey-London-Hong: World Scientific Publishing; 2000.

[136] Wagner, T., Dix, B., FriedeBurg, C. V., Frieß, U., Sanghavi, S., Sinreich, R., Platt, U.: MAX-DOAS O_4 measurements: A new technique to derive information on atmospheric aerosols-Principles and information content. J. Geophys. Res.: Atmos., 109, D22205, doi.org/10.1029/2004jd004904, 2004.

[137] Serdyuchenko, A., Gorshelev, V., Weber, M., Chehade, W., Burrows, J. P.: High spectral resolution ozone absorption cross-sections-Part 2: Temperature dependence. Atmos. Meas. Tech., 7, 625-636, doi:10.5194/amt-7-625-2014, 2014.

[138] Wang, Y., Lampel, J., Xie, P., Beirle, S., Li, A., Wu, D., Wagner, T.: Ground-based MAX-DOAS observations of tropospheric aerosols, NO_2, SO_2 and HCHO in Wuxi, China, from 2011 to 2014. Atmos. Chem. Phys., 17, 2189-2215, doi.org/10.5194/acp-17-2189-2017, 2017.

[139] Wang, Y., Apituley, A., Bais, A., Beirle, S., Benavent, N., Borovski, A., Bruchkouski, I., Chan, K. L., Donner, S., Drosoglou, T., Finkenzeller, H., Friedrich, M. M., Frieß, U., Garcia-Nieto, D., Gómez-Martín, L., Hendrick, F., Hilboll, A., Jin, J., Johnston, P., Koenig, T. K., Kreher, K., Kumar, V., Kyuberis, A., Lampel, J., Liu, C., Liu, H., Ma, J., Polyansky, O. L., Postylyakov, O., Querel, R., Saiz-Lopez, A., Schmitt, S., Tian, X., Tirpitz, J. L., Van Roozendeal, M., Volkamer, R., Wang, Z., Xie, P., Xing, C., Xu, J., Yela, M., Zhang, C., Wagner, T.: Inter-comparison of MAX-DOAS measurements of tropospheric HONO slant column densities and vertical profiles during the CINDI-2 campaign. Atmos. Meas. Tech., 13, 5087–5116, doi.org/10.5194/amt-13-5087-2020, 2020.

[140] Thalman, R., Volkamer, R.: Temperature dependent absorption cross-sections of O_2-O_2 collision pairs between 340 and 630 nm and at atmospherically relevant pressure. Phys. Chem. Chem. Phys., 15, 15371-15381, doi:10.1039/C3CP50968K, 2013.

[141] Vandaele, A. C., Hermans, C., Simon, P. C., Carleer, M., Colin, R., Fally, S., Merienne, M. F., Jenouvrier, A., Coquart, D.: Measurements of the NO_2 absorption cross-section from 42000 cm^{-1} to 10000 cm^{-1} (238–1000nm) at 220K and 294K. J. Quant. Spectrosc. Ra., 59, 171-184, doi:10.1016/S0022-4073(97)00168-4, 1998.

[142] Stutz, J., Kim, E. S., Platt, U., Bruno, P., Perrino, C., Febo, A.: UV-visible absorption cross sections of nitrous acid. J. Geophys. Res.: Atmos., 105, 14585-14592, doi:10.1029/2000JD900003, 2000.

[143] Aliwell, S. R., Van Roozendael, M., Johnston, P. V., Richter, A., Wagner, T., Arlander, D. W., Burrows, J. P., Fish, D. J., Jones, R. L., Tørnkvist, K. K., Lambert, J. C., Pfeilsticker, K., and Pundt, I.: Analysis for BrO in zenith-sky spectra: an intercomparison exercise for analysis improvement, J. Geophys. Res., 107, ACH 10-1–ACH 10-20, https://doi.org/10.1029/2001JD000329, 2002.

[144] Vandaele, A. C., Hermans, C., Simon, P. C., Carleer, M., Colin, R., Fally, S., Mérienne, M. F., Jenouvrier, A., and Coquart, B.: Measurements of the NO_2 absorption cross section from 42000 cm^{-1} to 10000 cm^{-1} (238–1000nm) at 220 K and 294 K, J. Quant. Spectrosc. Ra., 59, 171–184, doi:10.1016/S0022-4073(97)00168, 1998.

[145] Meller, R. and Moortgat, G. K.: Temperature dependence of the absorption cross sections of formaldehyde between 223 and 323 K in the wavelength range 225–375nm, J. Geophys. Res., 105, 7089–7101, doi:10.1029/1999JD901074, 2000.

[146] Volkamer, R., Spietz, P., Burrows, J., Platt, U.: High-resolution absorption cross-section of glyoxal in the UV-vis and IR spectral ranges, J. Photochem. Photobiol. A Chem., 172, 35–46, doi:10.1016/j.jphotochem.2004.11.011, 2005.

[147] Rothman, L. S., Gordon, I. E., Barbe, A., Benner, D. C., Bernath, P. E., Birk, M., Boudon, V., Brown, L. R., Campargue, A., Champion, J. P., Chance, K., Coudert, L. H., Dana, V., Devi, V. M., Fally, S., Flaud, J. M., Gamache, R. R., Goldman, A., Jacquemart, D., Kleiner, I., Lacome, N., Lafferty, W. J., Mandin, J. Y., Massie, S. T., Mikhailenko, S. N., Miller, C. E., Moazzen-Ahmadi, N., Naumenko, O. V., Nikitin, A. V., Orphal, J., Perevalov, V. I., Perrin, A., Predoi-Cross, A., Rinsland, C. P., Rotger, M., Simeckova, M., Smith, M. A. H., Sung, K., Tashkun, S. A., Tennyson, J., Toth, R. A., Vandaele, A. C., Vander Auwera, J.: The HITRAN 2008 molecular spectroscopic database, J. Quant. Spectrosc. Radiat. Transf., 110, 533–572, 2009.

[148] Fleischmann, O. C., Hartmann, M., Burrows, J. P., and Orphal, J.: New ultraviolet absorption cross-sections of BrO at atmospheric temperatures measured by time-windowing Fourier transform spectroscopy, J. Photoch. Photobio. A, 168, 117–132, 2004.

[149] Ward Jr, J. H.: Hierarchical grouping to optimize an objective function, J. Am. Stat. Assoc., 58, 236-244, 1963.

[150] Wang, Y., Zhang, X., Arimoto, R.: The contribution from distant dust sources to the atmospheric particulate matter loading at XiAn, China during spring, Sci. Total Environ., 368, 875-883, 2006.

24

983 [151] Cheng, S., Pu, G., Ma, J., Hong, H., Du, J., Yudron, T., Wagner, T.: Retrieval of tropospheric NO_2 vertical
984 column densities from ground-based MAX-DOAS measurements in Lhasa, a city on the Tibetan Plateau, Remote
985 Sens., 15, 4689, 2023a.
986 [152] Cheng, S., Ma, J., Zheng, A., Gu, M., Donner, S., Donner, S., Zhang, W., Du, J., Li, X., Liang, Z., Lv, J.,
987 Wagner, T.: Retrieval of O_3, NO_2, BrO and OClO columns from ground-based zenith scattered light DOAS
988 measurements in summer and autumn over the Northern Tibetan Plateau, Remote Sens., 13, 4242, 2021.
989 [153] Ma, J., Donner, S., Donner, S., Jin, J., Cheng, S., Guo, J., Zhang, Z., Wang, J., Liu, P., Zhang, G., Pukite, J.,
990 Lampel, J., Wagner, T.: MAX-DOAS measurements of NO_2, SO_2, HCHO, and BrO at the Mt. Waliguan WMO GAW
991 global baseline station in the Tibetan Plateau, Atmos. Chem. Phys., 20, 6973-6990, 2020.
992 [154] Cheng, S., Cheng, X., Ma, J., Xu, X., Zhang, W., Lv, J., Bai, G., Chen, B., Ma, S., Ziegler, S., Donner, S.,
993 Wagner, T.: Mobile MAX-DOAS observations of tropospheric NO_2 and HCHO during summer over the Three
994 Rivers' Source region in China, Atmos. Chem. Phys., 23, 3655-3677, 2023b.
995 [155] Li, M., Mao, J., Chen, S., Bian, J., Bai, Z., Wang, X., Chen, W., Yu, P.: Significant contribution of lightning
996 NO_x to summertime surface O_3 on the Tibetan Plateau, Sci. Total Environ., 829, 154639, 2022.
997
998